Macrophage ferroptosis potentiates GCN2 deficiency induced pulmonary venous arterialization

Jingyuan Zhang[1,2#], Pei Mao[1,2#], Tengfei Zhou[1,2#], Bingqing Yue[2, 4], Yaning Li[1,2], Yuanhua Qiu[3], Xianbao Liu[2], Fudi Wang[5, 6], Jingyu Chen[2,4,6], Jun Yang[1,2,6]

1. Department of Physiology and Department of Cardiology of the Second Affiliated Hospital, Zhejiang University School of Medicine, Hangzhou 310058, China.
2. State Key Laboratory of Transvascular Implantation Devices，Hangzhou 310009, China.
3. Department of Pulmonary and Critical Care Medicine, Shao Run Run Shaw Hospital, Zhejiang University School of Medicine, Hangzhou 310016, China.
4. Center for Lung Transplantation, Second Affiliated Hospital, Zhejiang University School of Medicine, Hangzhou 310052, China.
5. The Second Affiliated Hospital, School of Public Health，Zhejiang University School of Medicine, Hangzhou 310058, China.
6. These authors jointly directed this work.

[#] equal contribution

Correspondence: Jun Yang, yang_jun@zju.edu.cn

Summary

Haemosiderin-laden macrophages and the remodeling of pulmonary venules were found in Pulmonary veno-occlusive disease (PVOD), which is a fatal pulmonary vascular disease with deficient GCN2 expression, the underlying mechanism by which macrophage affects vascular cells, remains unclear. Here, we performed scRNA-sequencing analyses to show that macrophages were the major population affected by GCN2 deficiency and ferroptosis pathway-related genes were upregulated in lung macrophages from PVOD patients. Treatment with the specific ferroptosis inhibitor ferrostatin-1 (Fer-1) reversed the changes in haemodynamic indices observed in *Eif2ak4*$^{K1488X/K1488X}$ hypoxia mice and PVOD model rats. Furthermore, GCN2 deficiency increased HMOX-1 and iron levels to facilitate ferroptosis in macrophages and increased GCN2 deficiency-induced arterial marker expression in venous endothelial cells (VECs). Our findings suggest the potential of targeting macrophage ferroptosis as a therapeutic strategy for treating PVOD.

Key words

venous occlusion, macrophage ferroptosis, pulmonary venous

Introduction

In the lungs, macrophages are an abundant cell type that critically regulates normal homeostasis via the secretion of inflammatory factors and chemokines, which contribute to endothelium permeability and activation during the progression of vascular disease[1]. When increased inflammation and vascular permeability give rise to increased blood cells in the interstitial tissue, macrophages play important roles in clearance red blood cells to recycle iron[2]. Pulmonary veno-occlusive disease (PVOD) is a form of vascular disease characterized by haemosiderin-laden

macrophages and the remodeling of pulmonary venules which leads to pulmonary hypertension (PH)[3-5]. PVOD patients are typically diagnosed at a young age, and the mean time from diagnosis to death or need for lung transplantation is approximately one year[6]. *EIF2AK4* mutations have been found in all familial PVOD cases and in 9% of sporadic cases[6, 7]. However, general control nonderepressible 2 (GCN2) deficiency is not only caused by biallelic *EIF2AK4* mutations, but also been found in cancer patients after treatment with alkylating chemotherapeutic agents, such as cyclophosphamide and mytomycin-C (MMC) or even higher tobacco exposure[8]. Because the mechanism underlying the effects of GCN2 deficiency on pulmonary vascular remodeling is still unclear, lung transplantation remains the only available therapy for eligible patients[9]. Thus, novel evidence-based medical therapies for PVOD are needed[6, 10].

The *EIF2AK4* gene encodes GCN2 protein, a serine-threonine kinase that is upregulated in response to various cellular stresses[11]. GCN2 has been detected in pulmonary vessel walls and interstitial tissue, mostly in macrophages, of human lungs[12, 13]. Notably, reductions in GCN2 levels have been detected in the lungs of patients with both genetic and non-genetic forms of PVOD[6, 14]. However, to understand distinguishing changes in heterogeneous human endothelial cells (ECs), including artery, vein, and capillary ECs, can be challenging. These EC types have distinct molecular signatures and different physiological functions depending on their formation and microenviroment[15]. Whether GCN2 deficiency play specific roles in the macrophages and how the defected macrophages impact on VECs remain to be clarified.

Here, to identify the major affected cell types and key regulators involved in PVOD, we first performed single-cell RNA transcriptome sequencing (scRNA-seq) on lung samples collected from PVOD patients and from mitomycin-C -induced PVOD model rats (MMC rats). Surprisingly, we identified arterial markers expressed in remodeled veins surrounded by haemosiderin-laden macrophages in the lungs of PVOD patients[18]. Therefore, we hypothesized that GCN2 deficiency alters the endothelium by affecting the iron metabolism of macrophages in the pulmonary vascular niche[19]. Because the lack of an animal genetic model for *EIF2AK4* mutation-driven PVOD is one reason for the limited understanding of this disease[20, 21], we generated *Eif2ak4*$^{K1488X/K1488X}$ mice by knock in the human disease-causing mutation and PVOD patient-induced pluripotent stem cells (iPSCs) to recapitulate the pathogenesis observed in the lungs of PVOD patients[22]. These findings suggest the important role of macrophage ferroptosis in arterialization of the venous endothelium.

Results

Ferroptosis-related gene expression in lung macrophages is increased in PVOD patients with *EIF2AK4*^{mut}

We sought to clarify the role of GCN2 deficiency in the pathobiology of the pulmonary vasculature, especially the key factors that impact the development of occlusive venous structures. The patients had pathogenic characteristics of advanced PVOD with human *EIF2AK4* mutation in two alleles (Figure 1a). We carried out immunoblotting of GCN2 in lung tissues obtained from 5 control individuals and 5 patients bearing *EIF2AK4* mutations, which showed absence of GCN2 protein expression in the PVOD patients (Figure 1b). Consistent with the immunoblotting results, IHC analysis revealed that GCN2 was highly expressed in macrophages from the lung tissues of control individuals (Figure 1c). In agreement with a previous study[23], we also observed that the number of haemosiderin-laden macrophages was obviously increased in PVOD patients (Figure 1d).

Next we performed single-cell RNA sequencing (scRNA-seq) of explanted lung tissue samples

from two patients with confirmed *EIF2AK4*^{mut} PVOD (obtained after lung transplantation) to define the involved cell types and their roles in this disease. We obtained high-quality transcriptomic data from 12,128 single cells after stringent segregation[24], and integrated this dataset with data from three control samples to perform cell type annotation on the basis of a reference dataset from the Human Lung Cell Atlas (HLCA)[25]. All the samples presented similar cell type compositions and proportions (Figures 1e and S1a-S1d). To identify the cell population that was most affected by *EIF2AK4*^{mut}, we considered differences in cell–cell interactions to be potential sources of these phenotypic differences by comparing ligand-receptor interaction strengths among all the cell subtypes in the control individuals and PVOD patients. We found that the overall strength with which macrophages communicate with other cell types was significantly increased in PVOD patients (Figure 1f).

Differential gene expression enrichment and pathway scoring analysis of macrophages including alveolar macrophages (AMs), interstitial macrophages (IMs), and monocytes, from controls and PVOD patients revealed that ferroptosis-associated gene expression was highly increased in PVOD patients (Figures 1g and S1e). The degree of iron deposition, as determined by enhanced Perls' DAB staining, progressively increased in PVOD patients (Figures 1h and S1f). Iron is required for the accumulation of lipid peroxidation products to induce ferroptosis[26]. We observed substantial lung iron accumulation (Figures 1i and 1j) and lipid peroxidation, as evidenced by increased levels of MDA (Figure 1k) and 4-HNE (Figure 1l) expression in PVOD patients. These observations suggest that ferroptosis was induced in the lung macrophages of PVOD patients with *EIF2AK4*^{mut}.

Hypoxia induced-*Eif2ak4*$^{K1488X/K1488X}$ mice as a model for PVOD

To recapitulate the phenotype of PVOD, we generated a knock-in mouse strain that bears the same disease-causing mutation (a premature stop codon) in exon 33 of the endogenous *EIF2AK4* locus as PVOD 1 shown in Figure 1 (Figure 2a). Homozygous *Eif2ak4*$^{K1488X/K1488X}$ mice presented normal birth rates, although GCN2 protein expression in the lungs was reduced in these mice (Figure 2a). At 6 months of age, no detectable alterations in the right ventricular systolic pressure (RVSP), the extent of RVH or the total pulmonary vascular resistance index (TPVRI) were observed in *Eif2ak4*$^{K1488X/K1488X}$ mice compared with wild-type (WT) mice (Figures 2b-2d). To induce a severe pulmonary vascular phenotype, we introduced hypoxia as a trigger for capillary contraction and endothelium leakage (Figures S6a and S6b). After 6 weeks of hypoxia exposure, the TPVRI values were significantly greater in the *Eif2ak4*$^{K1488X/K1488X}$ mice than in the WT mice (Figure 2b), but the RVSP and the extent of RVH were not significantly different between the two groups (Figures 2c and 2d).

Histopathological analysis revealed the substantial infiltration of inflammatory cells around the pulmonary vein in *Eif2ak4*$^{K1488X/K1488X}$ mice under hypoxia (Figure 2e). Morphological analysis of vessels via α-SMA staining revealed initial narrowing within the pulmonary arterioles in hypoxia-induced WT and *Eif2ak4*$^{K1488X/K1488X}$ mice; strikingly, the muscularization of venules surrounded by inflammatory cells, indicating venous remodeling, was specifically detected in *Eif2ak4*$^{K1488X/K1488X}$ mice (Figures 2f and S6a). Greater muscularization of the pulmonary venules was also clearly present in hypoxia *Eif2ak4*$^{K1488X/K1488X}$ mice than in hypoxia-induced WT mice (Figure 2g).

We detected iron levels in whole-mouse-lung homogenates and found them to be significantly increased in *Eif2ak4K*$^{1488X/K1488X}$ mice under hypoxia (Figure 2h). Interestingly, heme-iron levels were significantly increased in hypoxic mice, but did not elevated in *Eif2ak4K*$^{1488X/K1488X}$ mice compared with control mice under hypoxia (Figure 2i). Consistent with the heme iron levels, we

found no significant difference in endothelium permeability between WT and *Eif2ak4K*$^{1488X/K1488X}$ mice under hypoxia (Figure S6b). This finding suggested that blood cells that leak through the endothelium are not the source of the elevated iron observed in mutant mouse lungs, another possibility could be that iron recycling is defective in mutant macrophages, leading to iron accumulation. Moreover, Perls' DAB staining revealed that macrophages in the lungs of *Eif2ak4K*$^{1488X/K1488X}$ mice presented greater levels of iron deposition than those in the lungs of WT mice under hypoxia did (Figure 2j). To confirm the occurrence of macrophage ferroptosis, we then measured lipid peroxidation in the lung tissue. Significantly elevated MDA levels (Figure 2k) and enhanced 4-HNE staining of macrophages (Figure 2l) were also observed in the lungs of *Eif2ak4K*$^{1488X/K1488X}$ mice under hypoxia. Moreover, we examined iron accumulation in other organs, including the kidney, liver, spleen and heart. Increased iron deposition was detected in the liver and spleen but not in the kidney or heart (Figure S6c). Taken together, these findings suggest that macrophages bearing the *Eif2ak4* mutation were refractory to iron recycling, which contributed to pulmonary venous remodeling in the mice.

Fer-1 reverses PVOD in *Eif2ak4*$^{K1488X/K1488X}$ hypoxia mice and MMC rats

To confirm the importance of macrophage ferroptosis in PVOD development, we examined the effects of the ferroptosis inhibitor ferrostatin-1 (Fer-1) in the PVOD mouse model. *Eif2ak4*$^{K1488X/K1488X}$ mice were reared under hypoxic or normoxic conditions for 6 weeks and treated with vehicle or Fer-1 either from the beginning of the hypoxia period (prevention protocol) or beginning on day 21 of hypoxia exposure (reversal protocol) (Figure 3a). We observed that Fer-1 treatment significantly reduced the TPVRI, RVSP and RVH in mice with both protocols (Figure 3b). Fer-1 reversed the histopathological phenotype of PVOD, including reductions in the pulmonary artery area, the venous lumen area and inflammatory cells infiltration (Figure 3c). Morphometric analysis and quantification of α-SMA staining revealed reduced thickening of the pulmonary artery and venous wall and muscularization of microvessels in the mice subjected to both protocols (Figures 3d and 3e). Together, these findings confirmed that ferroptosis inhibition reversed the PVOD phenotype in *Eif2ak4*$^{K1488X/K1488X}$ hypoxia mice.

To investigate whether macrophage ferroptosis, which was observed in the genetic form of PVOD, also occurs in non-genetic PVOD. We performed scRNA-seq on whole lung tissues from control rats and MMC-treated rats, an established model of disease in which reduction of GCN2 expression is a central feature (Figures S2a and S2b). These MMC rats exhibited typical phenotypes of PVOD, including reduced pulmonary artery and venous lumen areas and capillary haematomas (Figure S2f). A total of 24,156 cells from 4 samples (from 2 control rats and 2 MMC rats) were included after quality control (Figure S7). Combined Seurat analysis provided detailed classification of immune cells (Figure S2c). Enrichment scores for iron accumulation signatures (IAS) and ferroptosis gene sets were calculated, revealing significant elevation in macrophages, within the MMC group (Figures S2d and S2e). Iron levels in whole-lung homogenates were significantly increased in MMC-induced rats (Figures S2g and S2h). Macrophages had greater levels of iron deposition in the MMC than in control rat lungs (Figure S2j). Significantly elevated lipid peroxidation were also observed in the MMC rats (Figures S2i and S2k). Overall, consistent with our observations showed above, ferroptotic macrophages and accumulated iron in interstitium may induce the PVOD phenotype in MMC rats.

We examined the effects of Fer-1 in MMC-induced PVOD model rats[27]. The rats were given 3

mg/kg MMC (once per week for 2 weeks, i.p.) for 5 weeks, with or without Fer-1 administered either from the beginning of MMC treatment (prevention protocol) or starting on day 21 of MMC treatment (reversal protocol) (Figures 3f). Fer-1 reduced the TPVRI, RVSP and ameliorated RVH in rats treated with both prevention and reversal protocols (Figure 3g). Similarly, Fer-1 prevented or rescued the histopathological phenotype of PVOD, reducing the pulmonary artery and venous lumen areas and the incidence of capillary haematomas, in the treatment groups (Figure 3h). Morphometric analysis revealed reduced initial narrowing within pulmonary arteries, and quantification of α-SMA staining indicated alleviation of the muscularization of pulmonary veins and microvessels in rats treated with both the prevention and reversal protocols (Figures 3i and 3j).

GCN2 deficiency enhances HMOX-1 expression and promotes ferroptosis in macrophages

To identify the downstream mediator of GCN2, we performed on differentially expressed genes(DEGs) analysis of scRNA-seq data from macrophages and determined that *HMOX1* was among the top DEGs (Figure 4a). The protein encoded by *HMOX1*, heme oxygenase 1 (HMOX-1), catalyses the rate-limiting step in heme degradation to release iron, and an aberrant elevation in HMOX-1 levels may initiate ferroptosis under pathological conditions[28]. We performed Western blot analysis of HMOX-1 and the ferroptosis markers FTL, FTH and TFRC in all the PVOD patient lung homogenate tissue samples and observed significantly elevated protein expression compared with that in the control samples (Figures 4b and 4c). The expression of all of these factors was significantly increased in whole-lung tissue homogenates from MMC-treated rats (Figures 4e and 4f) and *Eif2ak4*$^{K1488X/K1488X}$ hypoxia mice (Figures 4h and 4i) and in *Eif2ak4*$^{K1488X/K1488X}$ bone marrow-derived macrophages (BMDMs) (Figures 4j and 4k). Increased HMOX-1 expression was also confirmed in GCN2 knockout HT1080 cells in the presence of additional iron (Figures S4a and S4b). However, the expression of other ferroptosis-related factors, including ACSL4, TXNRD1 and GPX4 were not significantly changed which excluded the possibility of the involvement of these factors (Figures S4b). Furthermore, the immunohistochemistry results confirmed that HMOX-1 was highly expressed in macrophages from PVOD patients and MMC-treated rats (Figures 4d and 4g).

These findings suggest that GCN2 deficiency renders macrophages more susceptible to ferroptosis. To investigate this hypothesis, we evaluated the effects of the ferroptosis activators ferric citrate (FAC) and RSL3 in BMDMs obtained from WT and *Eif2ak4*$^{K1488X/K1488X}$ mice. Furthermore, we generated *EIF2AK4* knockout HT1080 cells (a cell line sensitive to ferroptosis) via CRISPR/Cas9 targeted editing to examine the effects of ferroptosis activation in these cells and in control cells. Treatment with either FAC or RSL3 reduced cell viability in a dose-dependent manner in all the cells examined, and this ferroptosis-activating effect was stronger in the mutant cells than in the normal control cells (Figures 4l and S3a). BODIPY 581/591 staining revealed greater lipid peroxidation in response to FAC exposure in *Eif2ak4*$^{K1488X/K1488X}$ BMDMs than in WT BMDMs (Figure 4m). Moreover, we observed a significant increase in intracellular iron deposition in GCN2-deficient BMDMs and HT1080 cells following iron treatment (Figures 6g and 6h, Figure S4c and S4d). However, the GSH/GSSG ratio, an indicator of redox status, did not significantly change in human lung tissue or iron-treated cells (Figures S4e and S4f). These findings suggested that GCN2 deficiency sensitized macrophages to ferroptosis induction via increased HMOX-1 expression, especially under iron stimulation.

Previous studies have shown that GCN2 deficiency leads to recruitment of the transcription factor NRF2 to the *HMOX1* gene, resulting in elevated HMOX1 expression [29, 30]. Therefore, we analysed

the expression of NRF2 in BMDMs and HT1080 cells by immunoblotting. Consistent with previous findings, GCN2-deficient cells presented a significant increase in NRF2 expression under iron stimulation (Figures S5a-S5d). To examine whether HMOX1 could exaggerate the phenotype in our model mice, we challenged *Eif2ak4*$^{K1488X/K1488X}$ mice with the HMOX1 activator hemin. However, the stimulation of hypoxia-induced *Eif2ak4*$^{K1488X/K1488X}$ mice with hemin did not result in obvious PH phenotypes within 6 weeks (Figure S5e). The treatment of PVOD model mice and model rats with either an HMOX1 activator, hemin, or an HMOX1 inhibitor, Znpp, did not significantly promote or inhibit PVOD progression (Figures S5f and S5g). Collectively, these findings indicate that elevated levels of HMOX-1/FTL/FTH increase the susceptibility of GCN2-deficient macrophages to ferroptosis, but targeting HMOX1 alone is not desirable for the treatment of PVOD.

GCN2 deficiency enhances VEC arterialization and smooth muscle cell recruitment in the presence of iron

To investigate the effects of macrophages on the pulmonary vasculature, we next examined the DEGs in *EIF2AK4*^{mut} VECs in the lungs of PVOD patients. ScRNA-seq revealed that genes related to the arterial specification-related genes *NOTCH4* and *JAG2*, and the secretory marker *CXCL12* were highly upregulated in PVOD VECs compared with control VECs, whereas the venous development-related genes *TEK* and *NR2F2* presented reduced expression (Figure 5a). These finding suggest that venous arterialization may occur in the lungs of PVOD patients. We employed the CRISPR/Cas9 system to knock in the mutated *EIF2AK4* gene in HUVECs (GCN$^{-/-}$), the high efficiency of this process was confirmed (Figure 5d).

Screening for secretory factors in human lung macrophages via scRNA-seq revealed that TNFα were highly expressed (Figure 5b). The elevated expression of TNFα was validated by ELISA of homogenized human lung tissue and supernatants collected from iron-treated *Eif2ak4*$^{K1488X/K1488X}$ BMDMs (Figure 5c). In addition to the high levels of inflammatory factors in ferroptotic macrophage supernatants, iron can induce fibrosis in vascular disease, as recently reported[19, 31]. To examine the effect of iron on the vasculature, we conducted a Transwell study of human pulmonary smooth muscle cells (hPASMCs) with GCN2$^{-/-}$ HUVECs plated at the bottom well of the Transwell plate and observed an increase in hPASMC migration (Figures 5e and 5f). FAC treatment further increased the proliferation of hPASMCs (Figures 5e and 5g), which was not affected by the addition of iron to the culture medium (Figure 5h). Furthermore, we established a 3D HUVEC–hPASMC coculture assay to confirm the effect of iron on endothelial network formation. Compared with the control culture conditions, GCN2$^{-/-}$ HUVEC cocultures resulted an increase in the numbers of hPASMCs that wrapping around the ECs to provide physical support and for tube formation. Compared with control cultures, FAC-treated GCN2$^{-/-}$-HUVEC cocultures presented increases in the total endothelial network area, total cord length and number of branch points (Figure 5i).

To determine the direct effects of iron on the GCN2-deficient pulmonary vasculature in vivo, we administered intrapulmonary FAC to *Eif2ak4*$^{K1488X/K1488X}$ mice. HE staining of the lungs revealed the persistent infiltration of inflammatory cells and deposition of haemosiderin after 14 days of intrapulmonary iron administration. By day 35, the infiltration of inflammatory cells had decreased, but significant thickening of the blood vessel walls was observed (Figure 6a). Iron staining of the lung tissue revealed abundant iron deposition from days 14 to 21, particularly in macrophages. However, iron deposition gradually decreased after 35 days of iron administration (Figure 6b). Notably, the RVSP and the extent of RVH in the mice significantly increased after 14 days of iron

administration, but did not decrease after 35 days, despite the decrease in iron deposition (Figures 6c and 6d). Although there was no significant change in the thickness of the medial layer in the pulmonary arteries on day 35, significantly increased medial thickness in the pulmonary veins was observed (Figures 6e and 6f). In summary, GCN2 deficiency enhanced arterial marker gene expression in VECs and iron treatment promoted venous medial thickening in vitro and in vivo.

Discussion

We report here that GCN2 deficiency-induced macrophage ferroptosis contributes to venous arterialization in the pulmonary vasculature and that ferroptosis inhibitor can be used to reverse established venous remodeling in animal models of PVOD. This work also shows that mice bearing a human disease-causing mutation are susceptible to PVOD, providing a new model for this disease and clarifying the mechanism of macrophage ferroptosis drived venous arterialization.

In this study, we assessed ferroptosis-related gene expression in immune cells of PVOD patient and model rat lung tissues for the first time via scRNA-seq. These observations are consistent with haemosiderin accumulation in macrophages, a pathological characteristic of PVOD[32]. Furthermore, GCN2 was reported to control erythrocyte clearance and then affect iron recycling in mouse liver macrophages under stress[29]. However, mutation-bearing patients are most affected by pulmonary hypertension, thus, alterations in the oxygen supply are another important inducer for setting up relevant disease phenotypes in our mouse model.

In vitro and in vivo experiments confirmed increased HOMX1 expression in *Eif2ak4*-mutated macrophages[4], and we also demonstrated upregulation of its transcription factor NRF2 in mutant BMDMs and HT1080 cells. However, HMOX-1 inhibition did not reverse this PVOD phenotype in vivo. Since PVOD patients experience lung haemorrhage, increased *HMOX1* expression may be required for macrophages to clear extravascular red blood cells[33]. However, our results demonstrated that ferroptosis inhibition not only successfully prevented PVOD development, but also reversed established disease phenotype in *Eif2ak4*$^{K1488X/K1488X}$ mice and MMC rats, suggesting that macrophage ferroptosis inhibition could be an effective treatment strategy for the genetic and non-genetic forms of PVOD.

One limitation of the current study is the greater proportion of immune cells captured in our single-cell sequencing data, which resulted in a relatively reduced proportion of structural cells. In future studies, screening for the relevant disease types using this venous arterialization marker set to ensure that clinical trials involving ferroptosis inhibition are effective will be crucial.

Overall, we provide a new model to study ferroptotic macrophage drove venous arterialization in human disease. Our study builds on previous reports by clarifying the details of the interaction between macrophage defects and iron metabolic alterations in the pulmonary vascular niche, suggesting that targeting the macrophage ferroptosis is worth investigating for the treatment of PVOD and other related vascular diseases.

Acknowledgements

We thank Yu Zhou and Man Huang from ICU of Second Affiliated Hospital of Zhejiang University School of Medicine provided the patient sample storage and delivery. Dan Liu and Jing Feng from Tianjin General Hospital provided collaboration based clinical immunostaining training. X. Liang, help with the analysis of data. We also thank Shuangshuang Liu and Sanhua Fang from the Core Facilities, Zhejiang University School of Medicine for their technical support. This project received funding from the Nature

Science Foundation of China (81670054, 82470431, 82100364), the National Key Research and Development Program of China (2023YFC2507100, 2021YFA1100500), the China Postdoctoral Science Foundation (2022M712751).

Author contributions

J. Yang, design of the research studies, revision and finalization of the manuscript. J.Y. Zhang, conception, design, acquisition, analysis and interpretation of data and to the drafting of the article. P. Mao, help with design and the analysis of experiments related to iPSC vein endothelial differentiation. T.F. Zhou, help with the analysis of sc-RNA seq and 10X Visium transcriptome. F.D. Wang, providing supervision on iron metabolism study. B.Q. Yue, providing lung tissue samples of PVOD patients. Y.H. Qiu, providing patient information. J.Y. Chen, the major contribution on providing the PVOD patient samples and clinical information. All authors contributed to revision of the article.

Declaration interests

The authors declare no competing interests.

Reference

1. Guzik TJ, Nosalski R, Maffia P and Drummond GR. Immune and inflammatory mechanisms in hypertension. *Nat Rev Cardiol*. 2024;21:396-416.

2. Youssef LA, Rebbaa A, Pampou S, Weisberg SP, Stockwell BR, Hod EA and Spitalnik SL. Increased erythrophagocytosis induces ferroptosis in red pulp macrophages in a mouse model of transfusion. *Blood*. 2018;131:2581-2593.

3. Chaisson NF, Dodson MW and Elliott CG. Pulmonary Capillary Hemangiomatosis and Pulmonary Veno-occlusive Disease. *Clinics in Chest Medicine*. 2016;37:523-534.

4. Manaud G, Nossent EJ, Lambert M, Ghigna M-R, Boët A, Vinhas M-C, Ranchoux B, Dumas SJ, Courboulin A, Girerd B, Soubrier F, Bignard J, Claude O, Lecerf F, Hautefort A, Florio M, Sun B, Nadaud S, Verleden SE, Remy S, Anegon I, Bogaard HJ, Mercier O, Fadel E, Simonneau G, Vonk Noordegraaf A, Grünberg K, Humbert M, Montani D, Dorfmüller P, Antigny F and Perros F. Comparison of Human and Experimental Pulmonary Veno-Occlusive Disease. *American Journal of Respiratory Cell and Molecular Biology*. 2020;63:118-131.

5. Weatherald J, Dorfmüller P, Perros F, Ghigna M-R, Girerd B, Humbert M and Montani D. Pulmonary capillary haemangiomatosis: a distinct entity? *European Respiratory Review*. 2020;29:190168.

6. Montani D, Lau EM, Dorfmüller P, Girerd B, Jaïs X, Savale L, Perros F, Nossent E, Garcia G, Parent F, Fadel E, Soubrier F, Sitbon O, Simonneau G and Humbert M. Pulmonary veno-occlusive disease. *European Respiratory Journal*. 2016;47:1518-1534.

7. MANDEL J, MARK EJ and HALES CA. Pulmonary Veno-occlusive Disease. *American Journal of Respiratory and Critical Care Medicine*. 2000;162:1964-1973.

8. Ranchoux B, Günther S, Quarck R, Chaumais M-C, Dorfmüller P, Antigny F, Dumas SJ, Raymond N, Lau E, Savale L, Jaïs X, Sitbon O, Simonneau G, Stenmark K, Cohen-Kaminsky S, Humbert M, Montani D and Perros F. Chemotherapy-Induced Pulmonary Hypertension. *The American Journal of Pathology*. 2015;185:356-371.

9. Hadinnapola C, Bleda M, Haimel M, Screaton N, Swift A, Dorfmüller P, Preston SD, Southwood M, Hernandez-Sanchez J, Martin J, Treacy C, Yates K, Bogaard H, Church C, Coghlan G, Condliffe R,

Corris PA, Gibbs S, Girerd B, Holden S, Humbert M, Kiely DG, Lawrie A, Machado R, MacKenzie Ross R, Moledina S, Montani D, Newnham M, Peacock A, Pepke-Zaba J, Rayner-Matthews P, Shamardina O, Soubrier F, Southgate L, Suntharalingam J, Toshner M, Trembath R, Noordegraaf AV, Wilkins MR, Wort SJ, Wharton J, PAH NBRDCUNCSoIaH, Gräf S and Morrell NW. Phenotypic Characterization of EIF2AK4 Mutation Carriers in a Large Cohort of Patients Diagnosed Clinically With Pulmonary Arterial Hypertension. *Circulation*. 2017;136:2022-2033.

10. Humbert M, Kovacs G, Hoeper MM, Badagliacca R, Berger RMF, Brida M, Carlsen J, Coats AJS, Escribano-Subias P, Ferrari P, Ferreira DS, Ghofrani HA, Giannakoulas G, Kiely DG, Mayer E, Meszaros G, Nagavci B, Olsson KM, Pepke-Zaba J, Quint JK, Rådegran G, Simonneau G, Sitbon O, Tonia T, Toshner M, Vachiery J-L, Vonk Noordegraaf A, Delcroix M, Rosenkranz S and Group tEESD. 2022 ESC/ERS Guidelines for the diagnosis and treatment of pulmonary hypertension. *European Respiratory Journal*. 2023;61:2200879.

11. Donnelly N, Gorman AM, Gupta S and Samali A. The eIF2α kinases: their structures and functions. *Cellular and Molecular Life Sciences*. 2013;70:3493-3511.

12. Nossent EJ, Antigny F, Montani D, Bogaard HJ, Ghigna MR, Lambert M, Thomas de Montpréville V, Girerd B, Jaïs X, Savale L, Mercier O, Fadel E, Soubrier F, Sitbon O, Simonneau G, Vonk Noordegraaf A, Humbert M, Perros F and Dorfmüller P. Pulmonary vascular remodeling patterns and expression of general control nonderepressible 2 (GCN2) in pulmonary veno-occlusive disease. *The Journal of Heart and Lung Transplantation*. 2018;37:647-655.

13. Schupp JC, Adams TS, Cosme C, Raredon MSB, Yuan Y, Omote N, Poli S, Chioccioli M, Rose K-A, Manning EP, Sauler M, DeIuliis G, Ahangari F, Neumark N, Habermann AC, Gutierrez AJ, Bui LT, Lafyatis R, Pierce RW, Meyer KB, Nawijn MC, Teichmann SA, Banovich NE, Kropski JA, Niklason LE, Pe'er D, Yan X, Homer RJ, Rosas IO and Kaminski N. Integrated Single-Cell Atlas of Endothelial Cells of the Human Lung. *Circulation*. 2021;144:286-302.

14. Eyries M, Montani D, Girerd B, Perret C, Leroy A, Lonjou C, Chelghoum N, Coulet F, Bonnet D, Dorfmüller P, Fadel E, Sitbon O, Simonneau G, Tregouët D-A, Humbert M and Soubrier F. EIF2AK4 mutations cause pulmonary veno-occlusive disease, a recessive form of pulmonary hypertension. *Nature Genetics*. 2014;46:65-69.

15. Niklason L and Dai G. Arterial Venous Differentiation for Vascular Bioengineering. *Annual Review of Biomedical Engineering*. 2018;20:431-447.

16. Hou S, Li Z, Dong J, Gao Y, Chang Z, Ding X, Li S, Li Y, Zeng Y, Xin Q, Wang B, Ni Y, Ning X, Hu Y, Fan X, Hou Y, Li X, Wen L, Zhou B, Liu B, Tang F and Lan Y. Heterogeneity in endothelial cells and widespread venous arterialization during early vascular development in mammals. *Cell Research*. 2022;32:333-348.

17. Su T, Stanley G, Sinha R, D'Amato G, Das S, Rhee S, Chang AH, Poduri A, Raftrey B, Dinh TT, Roper WA, Li G, Quinn KE, Caron KM, Wu S, Miquerol L, Butcher EC, Weissman I, Quake S and Red-Horse K. Single-cell analysis of early progenitor cells that build coronary arteries. *Nature*. 2018;559:356-362.

18. Guzik TJ, Nosalski R, Maffia P and Drummond GR. Immune and inflammatory mechanisms in hypertension. *Nature Reviews Cardiology*. 2024;21:396-416.

19. Maus M, López-Polo V, Mateo L, Lafarga M, Aguilera M, De Lama E, Meyer K, Sola A, Lopez-Martinez C, López-Alonso I, Guasch-Piqueras M, Hernandez-Gonzalez F, Chaib S, Rovira M, Sanchez M, Faner R, Agusti A, Diéguez-Hurtado R, Ortega S, Manonelles A, Engelhardt S, Monteiro F, Stephan-Otto Attolini C, Prats N, Albaiceta G, Cruzado JM and Serrano M. Iron accumulation drives fibrosis,

senescence and the senescence-associated secretory phenotype. *Nature Metabolism*. 2023;5:2111-2130.
20. Zhang P, McGrath BC, Reinert J, Olsen DS, Lei L, Gill S, Wek SA, Vattem KM, Wek RC, Kimball SR, Jefferson LS and Cavener DR. The GCN2 eIF2α Kinase Is Required for Adaptation to Amino Acid Deprivation in Mice. *Molecular and Cellular Biology*. 2002;22:6681-6688.
21. Bignard J, Atassi F, Claude O, Ghigna M-R, Mougenot N, Abdoulkarim BS, Deknuydt F, Gestin A, Monceau V, Montani D, Nadaud S, Soubrier F and Perros F. T-cell dysregulation and inflammatory process in *Gcn2* (*Eif2ak4*$^{-/-}$)-deficient rats in basal and stress conditions. *American Journal of Physiology-Lung Cellular and Molecular Physiology*. 2023;324:L609-L624.
22. Chen Z, Zhang J, Wei D, Chen J and Yang J. GCN2 Regulates ATF3-p38 MAPK Signaling Transduction in Pulmonary Veno-Occlusive Disease. *Journal of Cardiovascular Pharmacology and Therapeutics*. 2021;26:677-689.
23. Zhang C, Lu W, Luo X, Liu S, Li Y, Zheng Q, Liu W, Wu X, Chen Y, Jiang Q, Zhang Z, Gu G, Chen J, Chen H, Liao J, Liu C, Hong C, Tang H, Sun D, Yang K and Wang J. Mitomycin C induces pulmonary vascular endothelial-to-mesenchymal transition and pulmonary veno-occlusive disease via Smad3-dependent pathway in rats. *British Journal of Pharmacology*. 2021;178:217-235.
24. Travaglini KJ, Nabhan AN, Penland L, Sinha R, Gillich A, Sit RV, Chang S, Conley SD, Mori Y, Seita J, Berry GJ, Shrager JB, Metzger RJ, Kuo CS, Neff N, Weissman IL, Quake SR and Krasnow MA. A molecular cell atlas of the human lung from single-cell RNA sequencing. *Nature*. 2020;587:619-625.
25. Sikkema L, Ramírez-Suástegui C, Strobl DC, Gillett TE, Zappia L, Madissoon E, Markov NS, Zaragosi L-E, Ji Y, Ansari M, Arguel M-J, Apperloo L, Banchero M, Bécavin C, Berg M, Chichelnitskiy E, Chung M-i, Collin A, Gay ACA, Gote-Schniering J, Hooshiar Kashani B, Inecik K, Jain M, Kapellos TS, Kole TM, Leroy S, Mayr CH, Oliver AJ, von Papen M, Peter L, Taylor CJ, Walzthoeni T, Xu C, Bui LT, De Donno C, Dony L, Faiz A, Guo M, Gutierrez AJ, Heumos L, Huang N, Ibarra IL, Jackson ND, Kadur Lakshminarasimha Murthy P, Lotfollahi M, Tabib T, Talavera-López C, Travaglini KJ, Wilbrey-Clark A, Worlock KB, Yoshida M, Chen Y, Hagood JS, Agami A, Horvath P, Lundeberg J, Marquette C-H, Pryhuber G, Samakovlis C, Sun X, Ware LB, Zhang K, van den Berge M, Bossé Y, Desai TJ, Eickelberg O, Kaminski N, Krasnow MA, Lafyatis R, Nikolic MZ, Powell JE, Rajagopal J, Rojas M, Rozenblatt-Rosen O, Seibold MA, Sheppard D, Shepherd DP, Sin DD, Timens W, Tsankov AM, Whitsett J, Xu Y, Banovich NE, Barbry P, Duong TE, Falk CS, Meyer KB, Kropski JA, Pe'er D, Schiller HB, Tata PR, Schultze JL, Teichmann SA, Misharin AV, Nawijn MC, Luecken MD and Theis FJ. An integrated cell atlas of the lung in health and disease. *Nature Medicine*. 2023;29:1563-1577.
26. Stockwell BR, Friedmann Angeli JP, Bayir H, Bush AI, Conrad M, Dixon SJ, Fulda S, Gascón S, Hatzios SK, Kagan VE, Noel K, Jiang X, Linkermann A, Murphy ME, Overholtzer M, Oyagi A, Pagnussat GC, Park J, Ran Q, Rosenfeld CS, Salnikow K, Tang D, Torti FM, Torti SV, Toyokuni S, Woerpel KA and Zhang DD. Ferroptosis: A Regulated Cell Death Nexus Linking Metabolism, Redox Biology, and Disease. *Cell*. 2017;171:273-285.
27. Dixon Scott J, Lemberg Kathryn M, Lamprecht Michael R, Skouta R, Zaitsev Eleina M, Gleason Caroline E, Patel Darpan N, Bauer Andras J, Cantley Alexandra M, Yang Wan S, Morrison B and Stockwell Brent R. Ferroptosis: An Iron-Dependent Form of Nonapoptotic Cell Death. *Cell*. 2012;149:1060-1072.
28. Ryter SW. Heme Oxgenase-1, a Cardinal Modulator of Regulated Cell Death and Inflammation. *Cells*. 2021;10:515.
29. Toboz P, Amiri M, Tabatabaei N, Dufour CR, Kim SH, Fillebeen C, Ayemoba CE, Khoutorsky A, Nairz M, Shao L, Pajcini KV, Kim K-W, Giguère V, Oliveira RL, Constante M, Santos MM, Morales

CR, Pantopoulos K, Sonenberg N, Pinho S and Tahmasebi S. The amino acid sensor GCN2 controls red blood cell clearance and iron metabolism through regulation of liver macrophages. *Proceedings of the National Academy of Sciences*. 2022;119:e2121251119.

30. Yuan J, Yu Z, Gao J, Luo K, Shen X, Cui B and Lu Z. Inhibition of GCN2 alleviates hepatic steatosis and oxidative stress in obese mice: Involvement of NRF2 regulation. *Redox Biology*. 2022;49:102224.

31. Fang X, Ardehali H, Min J and Wang F. The molecular and metabolic landscape of iron and ferroptosis in cardiovascular disease. *Nature Reviews Cardiology*. 2023;20:7-23.

32. Palazzini M and Manes A. Pulmonary veno-occlusive disease misdiagnosed as idiopathic pulmonary arterial hypertension. *European Respiratory Review*. 2009;18:177-180.

33. Garcia-Santos D, Hamdi A, Saxova Z, Fillebeen C, Pantopoulos K, Horvathova M and Ponka P. Inhibition of heme oxygenase ameliorates anemia and reduces iron overload in a β-thalassemia mouse model. *Blood*. 2018;131:236-246.

34. Zhou N, Yuan X, Du Q, Zhang Z, Shi X, Bao J, Ning Y and Peng L. FerrDb V2: update of the manually curated database of ferroptosis regulators and ferroptosis-disease associations. *Nucleic Acids Research*. 2023;51:D571-D582.

35. Vladimer Gregory I, Weng D, Paquette Sara WM, Vanaja Sivapriya K, Rathinam Vijay AK, Aune Marie H, Conlon Joseph E, Burbage Joseph J, Proulx Megan K, Liu Q, Reed G, Mecsas Joan C, Iwakura Y, Bertin J, Goguen Jon D, Fitzgerald Katherine A and Lien E. The NLRP12 Inflammasome Recognizes Yersinia pestis. *Immunity*. 2012;37:96-107.

RESOURCE AVAILABILITY

Lead contact

Further information and requests for resources and reagents should be directed to and will be fulfilled by the lead contact, **Jun Yang, yang_jun@zju.edu.cn**

Materials availability

All mouse lines are available from the lead contact with a completed Materials Transfer Agreement. **Data and code availability**

- Sequencing data will be made available on reasonable request.
- This paper does not report original code.
- Any additional information required to reanalyze the data reported in this paper is available from the lead contact upon request.

METHODS

Collection of Pulmonary Veno-Occlusive Disease (PVOD) Lung Tissue

Lung tissue samples from PVOD patients were obtained during lung transplantation procedures after written informed consent was obtained from all patients. The Institutional Review Boards (IRBs) of the Second Affiliated Hospital of Zhejiang University School of Medicine and Wuxi People's Hospital gave ethical approval for this work. The diagnosis of PVOD was confirmed via exome sequencing, which identified biallelic mutations in the *EIF2AK4* gene. The samples included multiple sections of proximal, middle, and distal lung tissue, each approximately 2 cm in size.

Single-Cell Transcriptomics

Lung tissue from two PVOD patients and two whole lungs each from mitomycin C (MMC)-treated and control rats

were processed. The tissue was minced, enzymatically digested, filtered, and washed before cell viability assessment (>80%) and loading into chromium microfluidic chips (3'v3 chemistry) for barcoding. Sequencing was performed via the Illumina HiSeq 2000 platform. The alignment was performed with Cell Ranger v6.0.0, and the human data were mapped to GRCh38, while the rat data were mapped to Rnor 6.0 reference genomes.

Seurat Analysis of scRNA-seq Data

The Seurat package (v4.3.0) was used for quality control, dimensionality reduction, and clustering. Cells expressing 500–5000 genes and with fewer than 15% mitochondrial gene expression but more than 3% ribosomal gene expression were retained. The human data were annotated using the HLCA dataset[25] and the azimuth method. The data were integrated with three normal lung scRNA-seq datasets using Harmony. Rat data were annotated using classic cell markers[24] and integrated with control and MMC-induced samples. Differentially expressed genes (DEGs) were identified using the 'FindMarkers' function with the Wilcoxon rank sum test. The expression of cell type-specific markers was determined using the COSG package.

Gene Set Enrichment Analysis (GSEA)

GSEA of the DEGs was conducted to supplement the ferroptosis gene set from FerrDb[34]. Single-sample gene set enrichment analysis (ssGSEA) was performed using the "escape" package. The "IAS" gene set from Maus et al. was used to assess the impact of iron on cellular populations[19].

MMC-Induced Rat Model

Five-week-old female Wistar rats (150–200 g) were randomly assigned to treatment groups. The control rats were given intraperitoneal injections of a control solution (50% PEG300 + 50% saline), whereas the MMC-treated rats received MMC (3 mg/kg, once a week for two weeks). Fer-1 (1 mg/kg) was administered intraperitoneally every other day, with the control group receiving saline. For the prevention model, saline or Fer-1 was given beginning on the first day of MMC treatment for 35 days. For the therapeutic model, treatment started on day 21 post-MMC treatment and continued every other day for 14 days. The HO-1 agonist hemin (25 mg/kg) and the HO-1 inhibitor Znpp (10 mg/kg) were administered intraperitoneally every other day for 35 days, starting from the first day of MMC treatment, with the control groups receiving saline or 50% PEG300 + 50% saline, respectively. All the experiments performed in the present study were approved by the Animal Institutional Review Boards (AIRB) of the Second Affiliated Hospital of the Zhejiang University School of Medicine (AIRB-2021-967).

Generation of Transgenic Mice

A guide RNA (gRNA) targeting exon 33 of *Eif2ak4* was designed with the sequence 5′-GCAAACAGAAAGCGTGTATTGG-3′ for use in CRISPR/Cas9. Cas9 mRNA, gRNA, and donor DNA were microinjected into fertilized eggs from C57BL/6J mice. The injected eggs were transferred to pseudopregnant surrogate mothers, resulting in the F0 generation. The F0 mice were genotyped, and those with positive results were mated with C57BL/6J mice to produce F1 offspring. F1 mice with the mutation c.4413-4416del were identified and bred to obtain homozygous mutants (*Eif2ak4*$^{K1488X/K1488X}$).

Hypoxia-Induced Mouse Model

Four-month-old C57BL/6J mice (25–30 g) were assigned to the following groups: the WT under normoxia, WT under hypoxia, *Eif2ak4*$^{K1488X/K1488X}$ under normoxia, and *Eif2ak4*$^{K1488X/K1488X}$ under hypoxia groups. Hypoxia treatment involved exposure to 10% oxygen for 6 weeks. Fer-1 (1 mg/kg) was administered intraperitoneally every other day; in the prevention model, Fer-1 was administered from the first day of hypoxia for 42 days, and in the

therapeutic model, Fer-1 was administered starting on day 21 for 21 days. Hemin (25 mg/kg) and Znpp (10 mg/kg) were administered intraperitoneally every other day, with the control groups receiving saline.

Intratracheal Administration of Iron to Mice

Ferric ammonium citrate (FAC, 50 mM) was administered intratracheally to 3-month-old C57BL/6J WT and *Eif2ak4*$^{K1488X/K1488X}$ mice[19]. The mice were anaesthetized with 0.15 mL of 1% sodium pentobarbital, and 10 μL of PBS/FAC was delivered intratracheally weekly for two weeks. Pulmonary function, the right ventricular systolic pressure (RVSP), right ventricular hypertrophy (RVH), and lung histology were evaluated four weeks after treatment initiation.

Haemodynamic Measurements in Rats and Mice

Identical methods were employed for haemodynamic measurements in both the rats and the mice. After the animals were anaesthetized, a catheter was inserted into the right ventricle via the right jugular vein to measure the RVSP. Continuous signals were collected using a physiological monitor for data analysis. To assess the RVH index, the hearts were dissected, and the right ventricle was isolated, washed with PBS, and weighed. The RVH index was calculated with the following formula: RVH index = (right ventricular weight/(left ventricle + septum weight)) × 100%. The total pulmonary vascular resistance index (TPVRI) was calculated using the following formula: TPVRI = RVSP (mmHg)/CI, where CI is RVCO (mL/min) * 100/body weight (g). The RVSP was measured via right heart catheterization, and the RVCO was estimated via echocardiography. For a statistical analysis of vascular remodeling, immunohistochemical staining of α-SMA was performed, and images were analysed using the VS200 system. Rat vessels (70–250 μm) and mouse vessels (50–150 μm) were analysed for lumen-to-total area ratios and media layer thickness, respectively. Microvessels were classified on the basis of α-SMA expression levels.

Immunohistochemical Staining

The paraffin-embedded sections were dewaxed, hydrated, and subjected to antigen retrieval. Endogenous peroxidase activity was quenched, and the sections were incubated with primary antibodies (against GCN2, 4-HNE, α-SMA, and HMOX1) overnight. Following secondary antibody incubation and DAB chromogen development, the sections were counterstained with haematoxylin, dehydrated, and mounted.

Prussian Blue Staining with DAB Enhancement

The paraffin-embedded sections were dewaxed and hydrated. The sections were then stained with 2% potassium ferrocyanide and 2% hydrochloric acid for 30 minutes, followed by three washes with distilled water. The chromogen DAB was applied for 5–10 minutes. The sections were counterstained with haematoxylin for 1 min, blued in PBS and rinsed with tap water. The sections were subsequently dehydrated in absolute ethanol, cleared in xylene, and mounted with neutral balsam.

Heme Quantification Assay

Heme was quantified using the Heme Iron Assay Kit (Abcam, ab272534). Tissue samples (0.1 g) were homogenized in 1 mL of PBS and centrifuged at 12,000 rpm for 10 minutes, after which the supernatants were collected. The assay wells received 50 μL of water (blank), the calibration solution, or a sample, followed by 200 μL of deionized water (blank/calibration wells) or reaction reagent (sample wells). The absorbance at 400 nm was measured after a 5-minute incubation period. The heme concentration was calculated as follows:

$$[heme] = \frac{(OD_sample \ - \ OD_blank)}{(OD_standard \ - \ OD_blank)} \times 62.5 \times n\mu M$$

Measurement of Tissue Non-heme Iron

Frozen lung tissue was sectioned, weighed, and digested in NHI acid at 65–70°C for ≥72 hours. The homogenized tissue was centrifuged at 12,000 rpm for 10 minutes. The supernatant was incubated with equal volumes of BAT buffer and a standard iron solution at room temperature for 10 minutes. The absorbance was read at 535 nm, after which the iron concentration was determined using a standard curve; the iron concentration is expressed as μg of iron per g of wet tissue.

Lipid Peroxidation (MDA) Assay

Lipid peroxidation was measured with an MDA Assay Kit (Biyuntian, S0131S). Frozen lung tissue (0.1 g) that had been homogenized in 1 mL of PBS was centrifuged at 12,000 rpm for 10 minutes. An MDA working solution was prepared and mixed with the lung homogenate, a standard, or PBS, followed by heating in a boiling water bath for 15 minutes. The samples were cooled and centrifuged, and the absorbance was measured at 532 nm and 450 nm.

Isolation and Culture of Murine Primary Bone Marrow-Derived Macrophages (BMDMs)

Femurs and tibias from euthanized mice were flushed with 1640 medium, and bone marrow cells were isolated. After red blood cell lysis, the cells were resuspended in differentiation types of medium (1640 medium, 10% serum, 15% L929 cell-conditioned medium) and plated. Differentiation was maintained by changing the medium every other day until day 7. BMDMs were harvested via 0.25% trypsin. For the cell viability and ferroptosis assays, BMDMs were treated with FAC or RSL3, and the staining assays were performed with BODIPY581/591[35].

Treatment of Endothelial Cells with Macrophage Supernatants

BMDMs differentiated for 7 days were treated with FAC for 24 or 48 hours, and the supernatants were collected. The supernatants were used with or without DFO to treat endothelial cells. For the 24Q group, BMDMs were treated with FAC, washed, and cultured for an additional 24 hours before the supernatant was collected.

Cultivation and Treatment of HT1080 Cells

HT1080 cells transfected with lentivirus and selected with puromycin were propagated in high-glucose medium supplemented with 10% FBS. For cell viability assays, the cells were treated with FAC or RSL3. For ferroptosis pathway detection, the cells were treated with FAC, and subsequent analyses included protein extraction, Per's DAB iron staining, and calcein assays.

Cultivation and Treatment of Endothelial Cells

Human umbilical vein endothelial cells (hUVECs) were cultured in ECM medium with 5% FBS. Lentivirus were used for GCN2 knockdown, which was confirmed by Western blotting. Endothelial cells were preconditioned in low-serum medium before treatment with FAC, TNFα. The cells were harvested for protein or RNA analysis following treatment.

Protein Extraction and Quantification and Western blotting

Protein extraction was performed using the Pierce™ BCA Protein Assay Kit (Thermo, 23227). Adherent cells were lysed in RIPA buffer and scraped, and the lysate was centrifuged at 12,000 rpm for 10 minutes. The tissue samples were homogenized in RIPA buffer and centrifuged in the same way. The supernatants were mixed with loading buffer, boiled, and stored at 4°C (short-term) or -80°C (long-term). Protein quantification was performed by mixing samples with a BCA working solution and measuring the absorbance at 562 nm after 30 minutes at 37°C. For Western blotting,

samples were loaded onto SDS–PAGE gels and separated at 110 V. Proteins were transferred to PVDF membranes at 300 mA for 2 hours. The membranes were blocked with QuickBlock™ Western Blocking Buffer for 30 minutes, incubated overnight at 4°C with primary antibodies, and washed. Secondary antibody incubation was performed for 2–3 hours at room temperature, followed by washing. Detection was performed using enhanced chemiluminescence (ECL) reagent.

RNA Extraction, Reverse Transcription, and Real-Time Quantitative PCR

Total RNA was extracted using TRIzol reagent (Genstar). The cells were lysed, mixed with chloroform, and centrifuged. The aqueous phase was mixed with isopropanol and incubated at -20°C overnight. The RNA was pelleted, washed with 75% ethanol, dried, and dissolved in RNase-free water. For reverse transcription, RNA was treated with gDNA Clean Reaction Mix and M-MLV reverse transcriptase. The mixture was incubated at 37°C for 15 minutes and 85°C for 5 seconds. Real-time quantitative PCR was performed using ChamQ Blue Universal SYBR qPCR Master Mix on a Roche Light Cycler 480 instrument. The PCR program consisted of predenaturation at 95°C for 3 minutes, followed by 45 cycles of 95°C for 10 seconds, 60°C for 30 seconds, and 72°C for 30 seconds. The data were analysed using Light Cycler 480 software.

Calcein Staining

Primary murine BMDMs and HT1080 cells were seeded in a 12-well plate and treated with 100 μM FAC for 24 hours. The cells were stained with calcein AM, incubated in the dark at 37°C for 10 minutes, and washed with PBS. The fluorescence intensity was measured using a microplate reader at an excitation wavelength of 494 nm and an emission wavelength of 524 nm.

GSH/GSSG Assay

Total and oxidized glutathione levels were measured using a GSH/GSSG Assay Kit (Beyotime, S0053). The tissue samples were homogenized and centrifuged, and the supernatant was used for the analysis. The samples were treated to remove GSH, and the absorbance at an OD of 412 nm was measured using prepared standards and reagents.

ELISAs

ELISAs for TNFα, GDF15, and CCL3 were conducted using specific kits (ABclonal). The tissue samples were homogenized, and the supernatants were collected. Standard curves were prepared, samples and standards were incubated with biotinylated antibodies and streptavidin-HRP, and the absorbance was measured at OD450 nm with a reference at OD630 nm using a microplate reader.

Statistics and Reproducibility

Statistical analysis was conducted using GraphPad Prism v9.0.0 or R software v4.2.3. The figure legends or Methods sections detail the statistical tests conducted and the repeat numbers. P value < 0.05 was considered statistically significant unless otherwise stated.

Figure

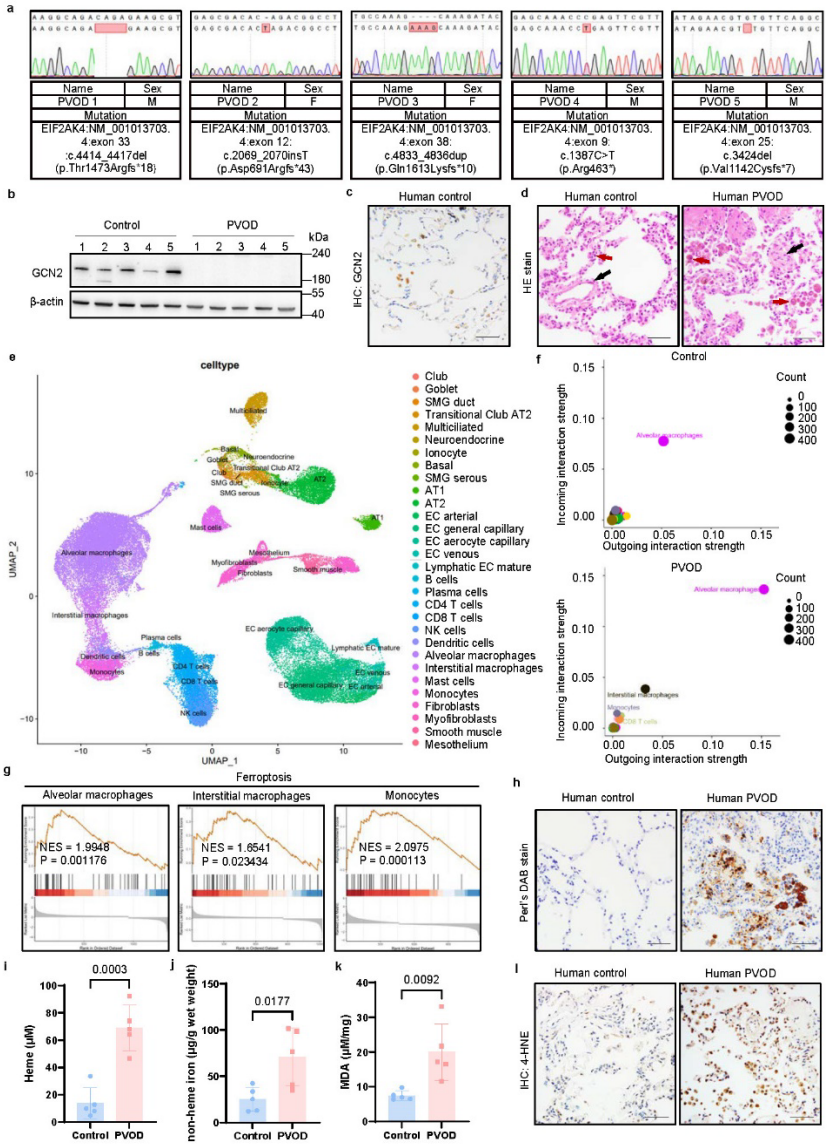

Figure 1. Ferroptosis-related gene expression within lung macrophages is enhanced in *EIF2AK4*^{mut} PVOD patients.

a, DNA sequencing analysis of tissues from pulmonary veno-occlusive disease (PVOD) patients in this study confirms EIF2AK4 mutations. **b**, Western blot showing the expression levels of GCN2 in control or PVOD patient lung tissues; n=5. **c**, Representative images from IHC analysis of GCN2 expression in control lung tissues. Scale bar=50 μm. **d**, Representative images of lung tissues stained with haematoxylin and eosin (H&E). Red arrow: macrophages; Black arrow: pulmonary vein. Scale bar=50 μm. **e**, UMAP projection showing the main cell type identified by integrated clustering analysis of scRNA-seq datasets from three controls and two *EIF2AK4*^{mut}-associated PVOD patients. **f**, Bubble plot showing the incoming and outgoing interaction strengths for each subpopulation of immune cells in the control and PVOD groups. The dot size represents the number of interactions. **g**, GSEA of differentially expressed genes in alveolar macrophages, interstitial macrophages, and monocytes between the control and PVOD groups. The ferroptosis-associated gene set was obtained from FerrDb. NES, normalized enrichment score. **h**, Control and PVOD patient lung tissues were stained with Perls' DAB to label ferric iron deposits. Scale bar=50 μm. **i**, Haem iron levels in the lungs of control and PVOD patients were measured. **j**, Nonhaem iron levels in the lung were measured in controls and PVOD patients. **k**, The MDA content in the lungs of control and PVOD patients was measured. **l**, Representative images of IHC analysis of 4-HNE content in control and PVOD patient lung tissues. Scale bar=50 μm. The data are presented as the means ± s.e.m. (n=5); unpaired two-tailed t test.

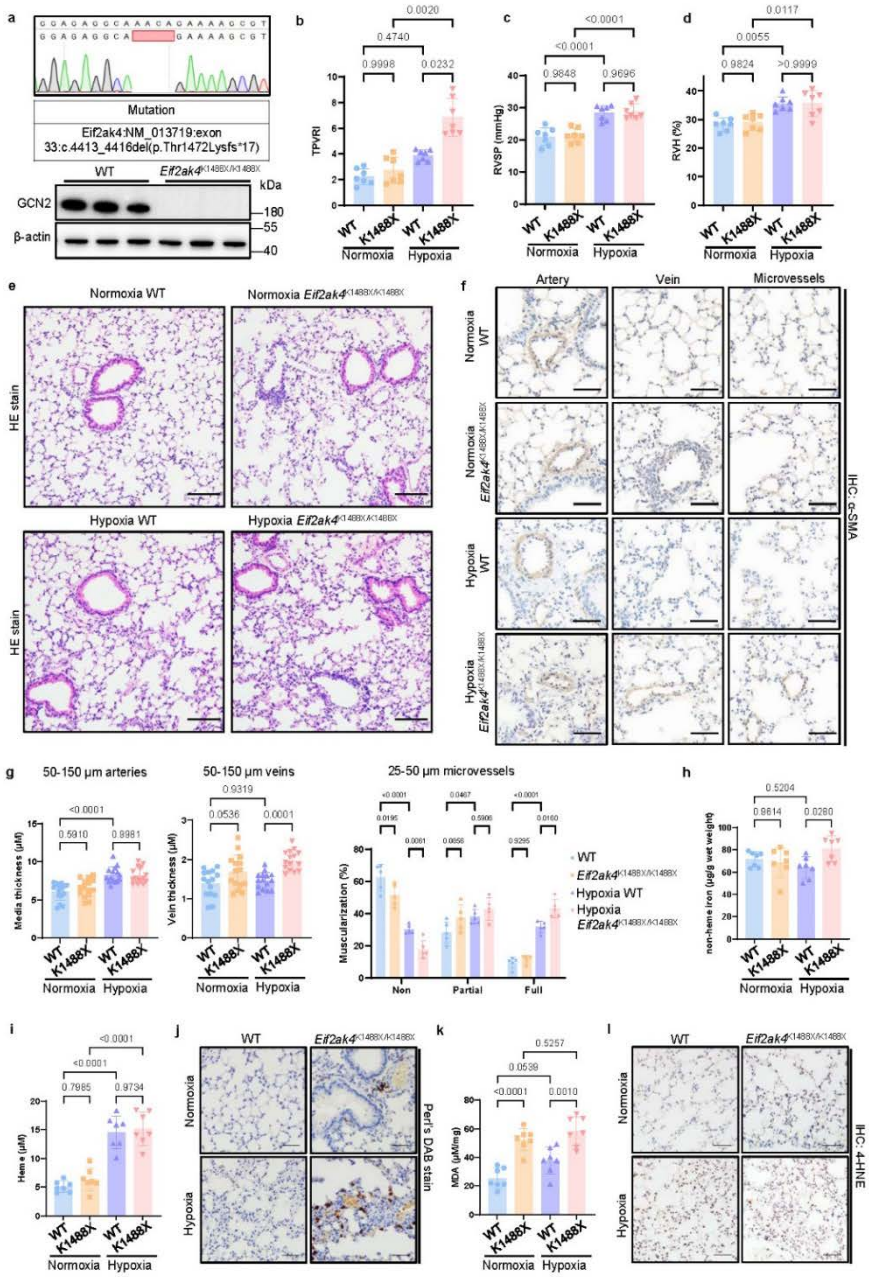

Figure 2. Hypoxia induced-*Eif2ak4*$^{K1488X/K1488X}$ mice as a model for PVOD.

a, DNA sequencing analysis of *Eif2ak4*$^{K1488X/K1488X}$ mice confirming the *EIF2AK4* mutation. Western blot revealing decreased expression of GCN2 in *Eif2ak4*$^{K1488X/K1488X}$ mouse lung tissues (n=3). **b-d**, Wild-type (WT) and *Eif2ak4*$^{K1488X/K1488X}$ (K1488X) mice were subjected to normoxia or hypoxia for 6 weeks. TPVRI value, RVSP and RVH extent in the model mice (n=7). **e**, Representative images of H&E-stained samples from the model mice. Scale bar=100 μm. **f**, Representative images of α-SMA staining of pulmonary arteries, veins and microvessels. Scale bar=50 μm. **g**, Medial thickness of pulmonary arteries (n=15), medial thickness of pulmonary veins (n=15), and muscularization (%) of microvessels (n=5) in the model mice. **h**, Non-heme iron levels in the lungs of the mice were measured. **i**, Heme iron levels in the lungs of the mice were measured. **j**, Ferric iron deposits in the model mice were stained with Perls' DAB. Scale bar=50 μm. **k**, MDA content in the lungs of the mice was measured. **l**, Representative images of 4-HNE staining in mice. Scale bar=50 μm. The data are presented as the means ± s.e.m.; two-way ANOVA with Tukey's multiple comparison test.

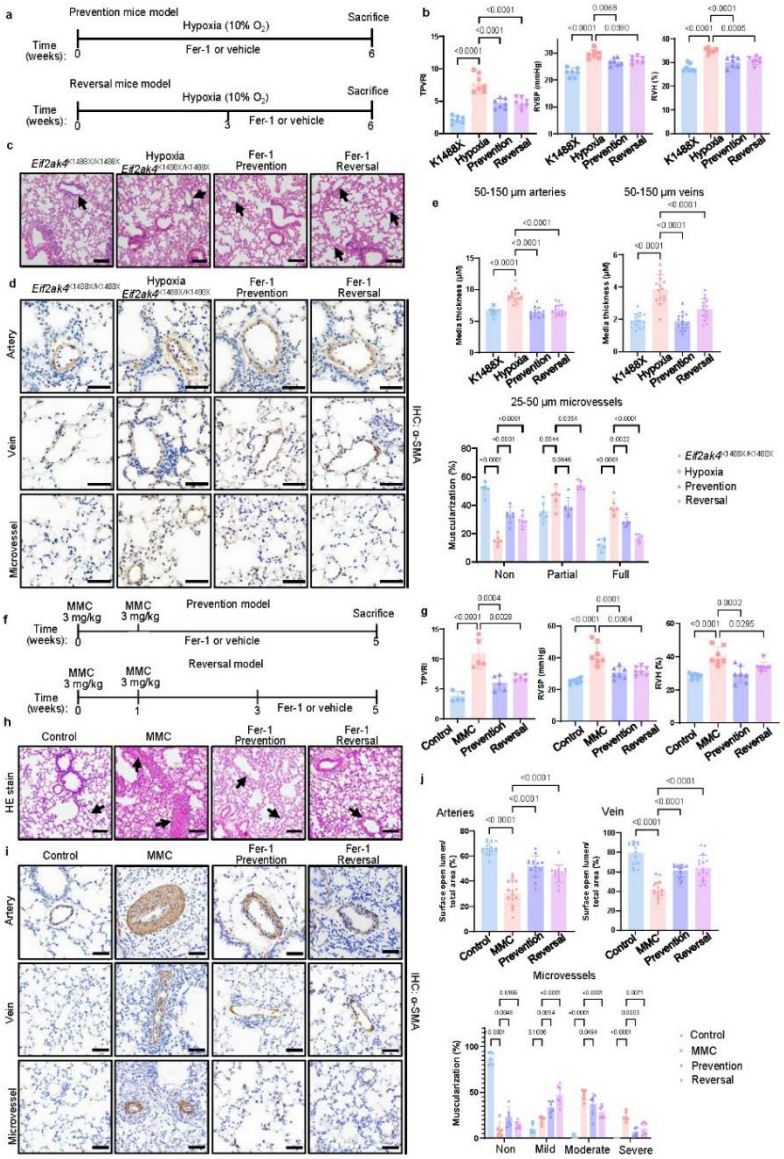

Figure 3. Fer-1 reverses PVOD in *Eif2ak4*$^{K1488X/K1488X}$ hypoxia mice and MMC rats

a, Schematic of the experimental design. *Eif2ak4*$^{K1488X/K1488X}$ mice (K1488X) were subjected to hypoxic or normoxic conditions for 42 days and treated with vehicle or Fer-1 from the start of the hypoxia treatment (prevention protocol) or beginning at 21 days (reversal protocol). **b**, Assessment of TPVRI, RVSP and RVH extent in the mice (n=7) described in a. **c**, Representative images of H&E-stained lung sections from the mice described in f. Pulmonary veins (arrows), scale bar=100 μm. **d**, Representative images of α-SMA staining in lung sections from the mice described in f. Scale bar=50 μm. **e**, Medial thickness of pulmonary arteries (n=15), medial thickness of pulmonary veins (n=15), and muscularization (%) of microvessels (n=6) in the mice described in f. The data are presented as the means ± s.e.m.; one-way ANOVA with Tukey's multiple comparison test. **f**, Schematic of the experimental design. The rats were given 3 mg/kg mitomycin-C (MMC) (once per week for 2 weeks, i.p.) or vehicle for 5 weeks and Fer-1 or saline from the start of the MMC treatment (prevention protocol) or beginning at 21 days (reversal protocol). **g**, Assessment of TPVRI, RVSP and RVH extent in the rats (n=7) described in a. **h**, Representative images of H&E-stained lung sections from the rats described in a. Pulmonary veins (arrows), scale bar=100 μm. **i**, Representative images of α-SMA staining in the pulmonary arteries, veins and microvessels of the rats described in a. Scale bar=50 μm. **j**, Surface open lumen/total area (%) of pulmonary arteries and veins (n=15) and muscularization (%) of microvessels (n=6) in the rats described in a.

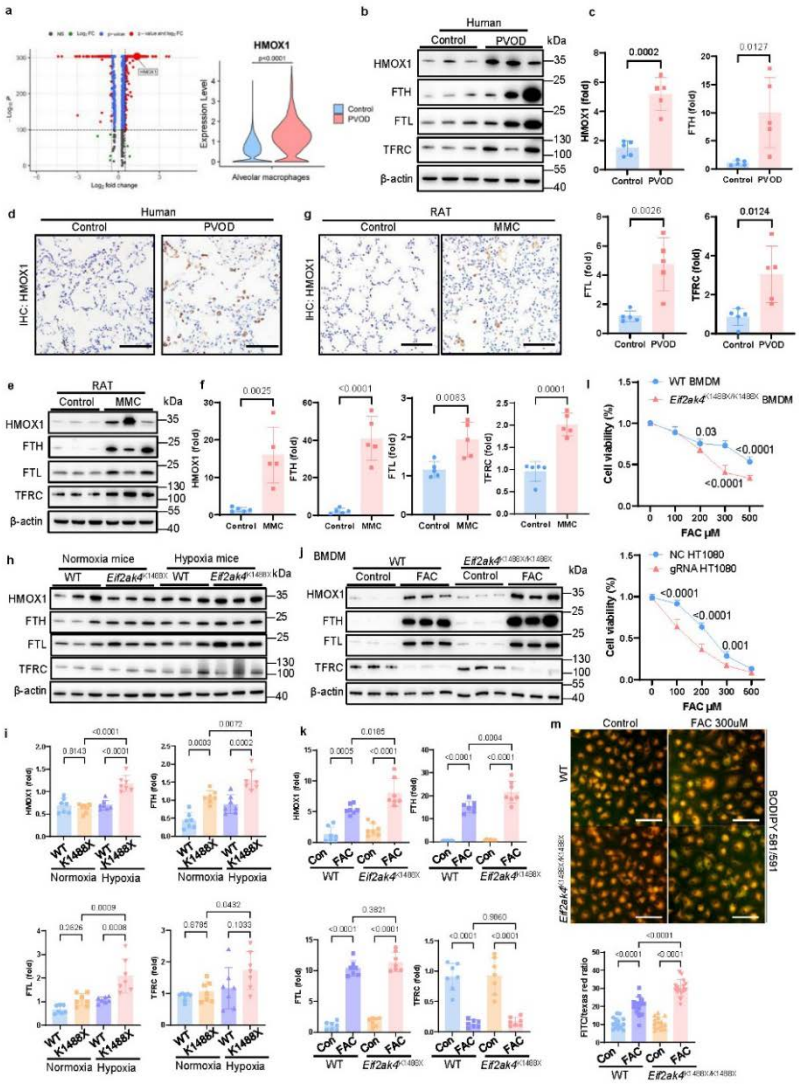

Figure 4. GCN2 deficiency enhances HMOX-1 expression and promotes ferroptosis in macrophages.

a, Volcano plot depicting the differentially expressed genes in alveolar macrophages from PVOD patients and controls. The violin plot highlights HMOX1 expression, identified as significantly different. P values were determined via the Wilcoxon method. **b-c**, Western blot and quantification of HMOX1, FTH, FTL, and TFRC in control and PVOD lung tissues. Data are presented as the means ± s.e.m. (n=5); unpaired two-tailed t test. **d**, Representative images of HMOX1 in control and PVOD patient lung tissues. Scale bar=50 μm. **e-f**, Western blot of HMOX1, FTH, FTL, and TFRC in control and MMC-treated rat lungs. Data are presented as the means ± s.e.m. (n=5); unpaired two-tailed t test. **g**, Representative images of HMOX1 staining in control and MMC-treated rat lung tissues. Scale bar=50 μm. **h-i**, WT and *Eif2ak4*$^{K1488X/K1488X}$ mice were subjected to hypoxia for 6 weeks. Western blot of HMOX1, FTH, FTL, and TFRC in mouse lungs. Data are presented as the means ± s.e.m. (n=7); two-way ANOVA. **j-k**, Western blot of HMOX1, FTH, FTL and TFRC in WT or *Eif2ak4*$^{K1488X/K1488X}$ BMDMs treated with or without 300 μM FAC for 24 h. Data are presented as the means ± s.e.m. (n=7); two-way ANOVA. **l**, Cell viability was measured in WT and *Eif2ak4*$^{K1488X/K1488X}$ BMDMs treated with the indicated concentrations of FAC for 48 h and in control (NC) and GCN2$^{-/-}$ (gRNA) HT1080 cells treated with the indicated concentrations of FAC for 24 h. Data are presented as the means ± s.e.m. (n = 6); unpaired multiple t tests. **m**, Lipid peroxidation in BMDMs treated with FAC for 12 h, assayed using BODIPY 581/591 dye. Representative microscopy images shown. Scale bar=50 μm. The data are presented as the means ± s.e.m. (n=15); two-way ANOVA.

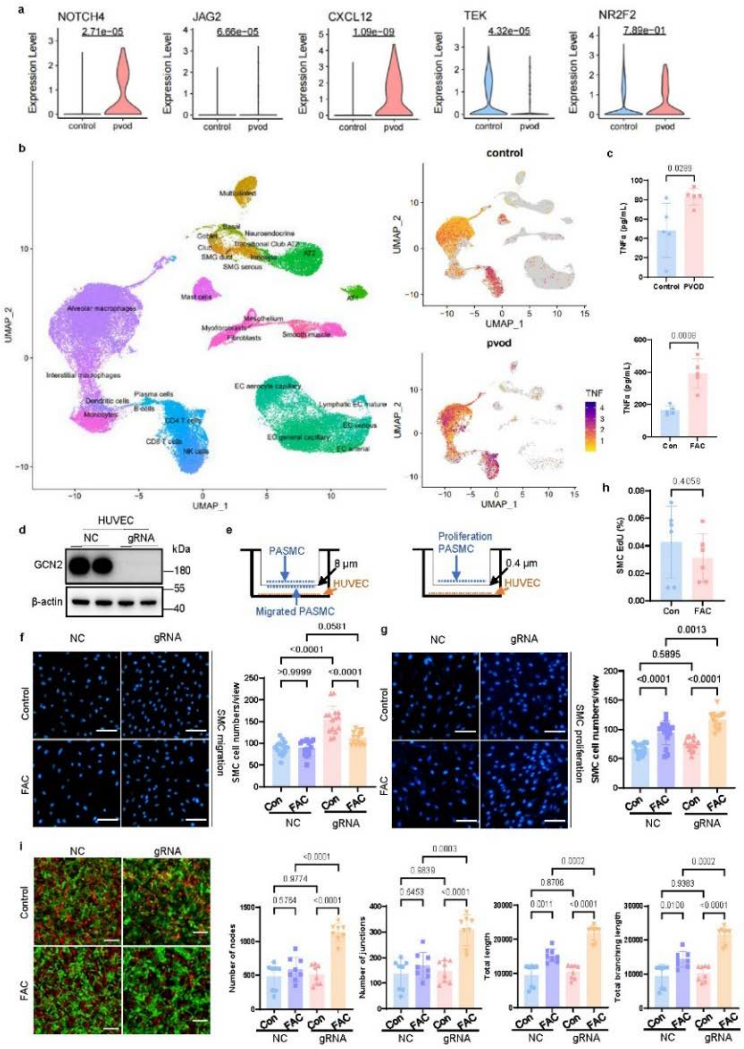

Figure 5. GCN2 deficiency enhances VECs arterialization and smooth muscle cell recruitment in the presence of iron. **a**, Violin plots highlighting the differentially expressed genes associated with arterial and venous identity in venous endothelial cells from human scRNA-seq data. P values were calculated via the Wilcoxon rank sum test. **b**, Feature plots depicting the expression of TNFα in human scRNA-seq data across control and PVOD groups are presented. The UMAP plot provides cell type annotations.**c**, ELISA results depict the concentrations of TNFα in lung tissues from control and PVOD patients, and the levels of TNFα in *Eif2ak4*$^{K1488X/K1488X}$ BMDM treated with/without 300 μM FAC 24 h. Data are the mean ± s.e.m., n=5, unpaired two-tailed t-test. **d**, WB showing expression levels of GCN2 in NC or GCN2$^{-/-}$ HUVECs. **e**, Schematic of the Transwell coculture model. NC/GCN2$^{-/-}$ HUVECs were seeded in the bottom compartment and treated ± 660 μM FAC for 72 h, with PASMCs seeded on top for 24 h. An 8-μm pore membrane facilitates migration; a 0.4-μm membrane tests proliferation. **f**, Images and quantification of DAPI-stained SMCs cocultured with control or GCN2$^{-/-}$ HUVECs in an 8-μm pore size chamber in FAC-treated medium indicating the migration ability of SMCs. Scale bar=100 μm. Data are presented as the means ± s.e.m. (n=15); two-way ANOVA. **g**, Images and quantification of DAPI-stained SMCs cocultured with control or GCN2$^{-/-}$ HUVECs in a 0.4-μm pore size chamber in FAC-treated medium revealing the proliferative ability of the SMCs. Scale bar=100 μm. The data are presented as the means ± s.e.m. (n=15); two-way ANOVA. **h**, Ratio of EdU-positive PASMCs after treatment ± 660-μM FAC for 24 h. Data are presented as the means ± s.e.m. (n=6); unpaired two-tailed t test. **i**, Representative images of HUVECs (green) cocultured with SMCs (PKH26, red) for 4 days. Scale bar=100 μm. Quantification of total network area, total cord length, and branch points. Data are presented as the means ± s.e.m. (n=8); two-way ANOVA.

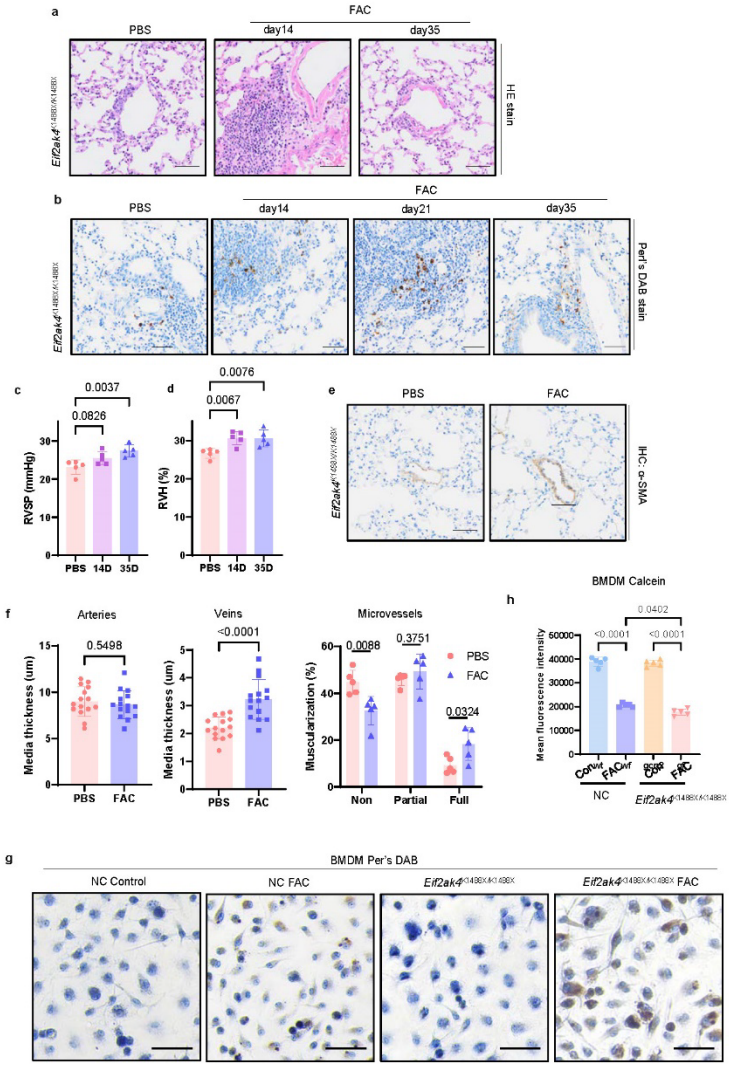

Figure 6. Intratracheal iron treated *Eif2ak4*$^{K1488X/K1488X}$ mice showed PVOD phenotype.

a, Representative images of H&E staining in lung sections from *Eif2ak4*$^{K1488X/K1488X}$ mice post-PBS or 500 nM FAC 14/35 days. Scale bar=50 µm. **b**, Ferric iron deposits were stained with Perls' DAB staining in *Eif2ak4*$^{K1488X/K1488X}$ mice post-PBS or 500 nM FAC 14/21/35 days. Scale bar=50 µm. **c-d**, Assessment of RVSP and RVH in *Eif2ak4*$^{K1488X/K1488X}$ mice post-PBS or 500 nM FAC 14/35 days. Data are the mean ± s.e.m., n=5, one-way ANOVA. **e**, Representative images of α-SMA in the pulmonary veins from *Eif2ak4*$^{K1488X/K1488X}$ mice post-PBS or 500 nM FAC 35 days. Scale bar=50 µm. **f**, Medial thickness of arteries and veins (n=15), and muscularization (%) of microvessels (n=5) in *Eif2ak4*$^{K1488X/K1488X}$ mice post-PBS or 500 nM FAC 35 days. Data are the mean ± s.e.m., unpaired two-tailed t-test. **g**, Ferric iron deposits were stained with Perls' DAB staining in WT or *Eif2ak4*$^{K1488X/K1488X}$ BMDMs treated with/without FAC 300 µM for 24h. Scale bar=50 µm. **h,** Mean fluorescence intensity of calcein assay in WT or *Eif2ak4*$^{K1488X/K1488X}$ BMDMs treated with/without FAC 300 µM for 24h. Data are the mean ± s.e.m., n=5, two-way ANOVA.

Supplemental information

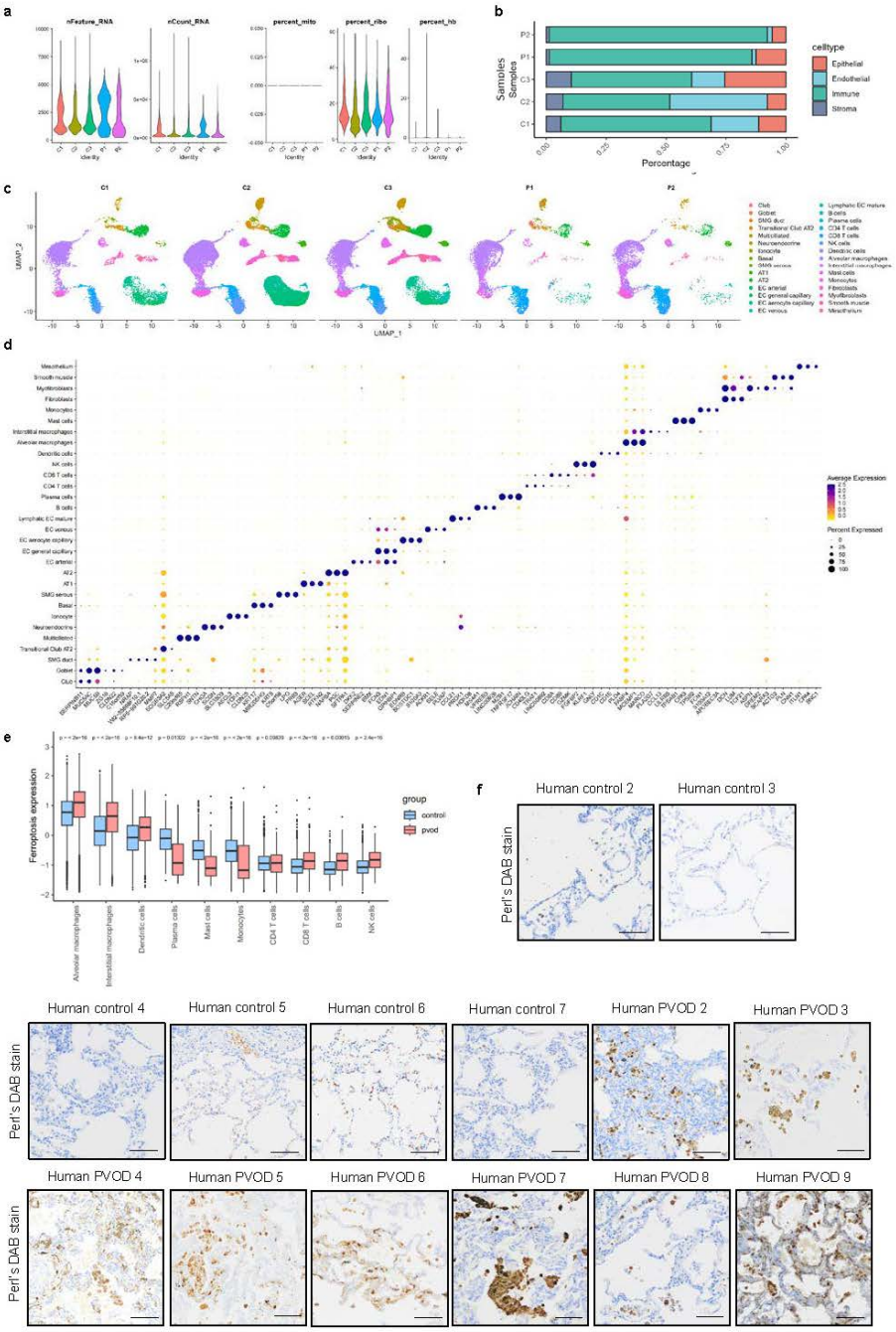

Figure S1. Quality control for human scRNA-seq data and detection of iron accumulation in patient lungs.
a, Violin plots depicting gene counts and unique molecular identifier (UMI) counts per droplet, alongside the proportions of mitochondrial, ribosomal, and erythrocyte gene-associated UMI counts within each droplet. **b**, Stacked bar plots showing proportions of main cell types detected in control and PVOD samples. **c**, UMAP plots of scRNA-seq data from control and PVOD groups, annotated with cell type labels. **d**, Dot plot depicting the expression levels of the top three marker genes for each cell type, as determined by the COSG method. **e**, Bar plot illustrating the enrichment scores of ferroptosis-related gene sets (derived from the FerrDb database) for each immune cell subtype, as computed by the ssGSEA algorithm, in both control and PVOD groups. This analysis was conducted using the "escape" package, with differential calculations performed via the Wilcoxon rank-sum test. **f**, Ferric iron deposits were stained with Perls' DAB staining in controls (control samples 2-7) and PVOD patients (PVOD samples 2-9) lung tissues. Scale bar=50 μm.

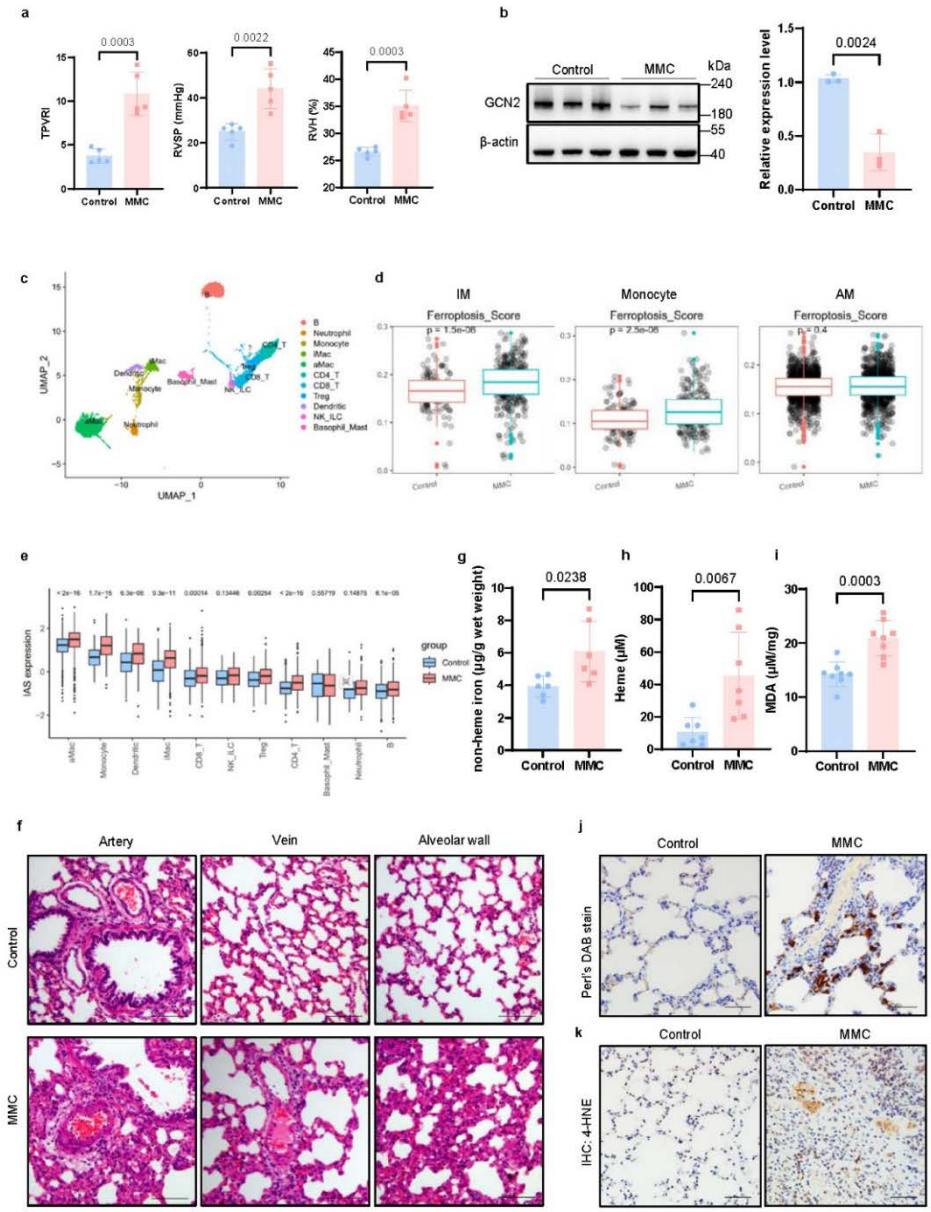

Figure S2. Ferroptosis and iron accmulation in lung macrophages from MMC-induced PVOD model rats.

a, RVSP, TPVRI and RVH in control and MMC-treated rats (n=5). **b**, Western blot showing decreased expression of GCN2 in lung tissues from MMC-treated rats (n=3). **c**, UMAP plot illustrating the subpopulations within the major immune categories derived from the integrated scRNA-seq data of samples from control and MMC-treated rats. **d**, Bar plot depicting the IAS gene set scores corresponding to the control and MMC groups within each subpopulation. P values were determined via the Wilcoxon method. **e**, Box plots illustrating the ferroptosis scores of alveolar macrophages, interstitial macrophages, and monocytes in the control and MMC-treated groups. The ferroptosis score was calculated in Seurat. P values were determined via the Wilcoxon method. **f**, Representative H&E-stained images showing pulmonary artery, vein and alveolar wall in control and MMC-treated rats. Scale bar=50 μm. **g**, Nonheme iron levels in the lungs of control and MMC-treated rats (n=6) were measured. **h**, Haem iron levels in the lungs of control and MMC-treated rats (n=7) were measured. **i**, The MDA content in the lungs of control and MMC-treated rats (n=8) was measured. **j**, Ferric iron deposits in lung samples from control and MMC-treated rats were stained with Perls' DAB. Scale bar=50 μm. **k**, Representative images of 4-HNE staining in control and MMC-treated rat lung tissues. Scale bar=50 μm. The data are presented as the means ± s.e.m.; unpaired two-tailed t test.

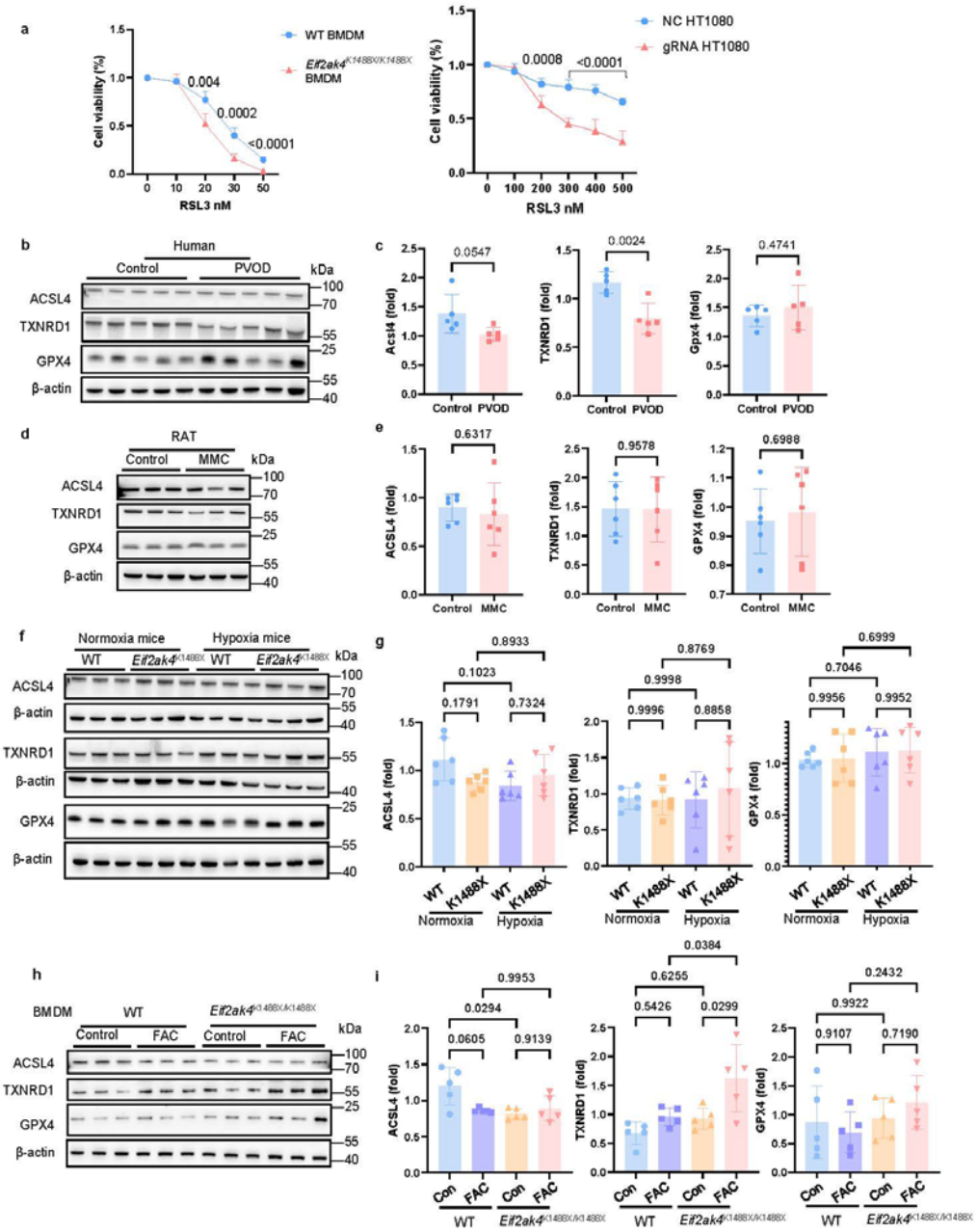

Figure S3. GCN2 deficiency has no effect on other ferroptosis pathways in PVOD patients and animal models.
a, Cell viability was measured in WT and *Eif2ak4*$^{K1488X/K1488X}$ BMDMs after treatment with indicated concentration of RSL3 for 24 h (n=5). Cell viability was measured in control (NC) and GCN2$^{-/-}$ (gRNA) HT1080s after treatment with indicated concentration of RSL3 for 24 h (n=6). Data are the mean ± s.e.m., multiple unpaired t test. **b-c**, WB showing expression levels of ACSL4, TXNRD1 and GPX4 in controls or PVOD patients lung tissues. Data are the mean ± s.e.m., n=5, unpaired two-tailed t-test. **d-e**, WB showing expression levels of ACSL4, TXNRD1 and GPX4 in controls or MMC-induced rats lung tissues. Data are the mean ± s.e.m., n=6, unpaired two-tailed t-test. **f-g**, WT and *Eif2ak4*$^{K1488X/K1488X}$ mice treated with/without hypoxia for 6 weeks. WB showing expression levels of ACSL4, TXNRD1 and GPX4 in mice lung tissues. Data are the mean ± s.e.m., n=6, two-way ANOVA. **h-i**, WB showing expression levels of ACSL4, TXNRD1 and GPX4 in WT or *Eif2ak4*$^{K1488X/K1488X}$ BMDMs treated with/without FAC 300 μM for 24h. Data are the mean ± s.e.m., n=5, two-way ANOVA.

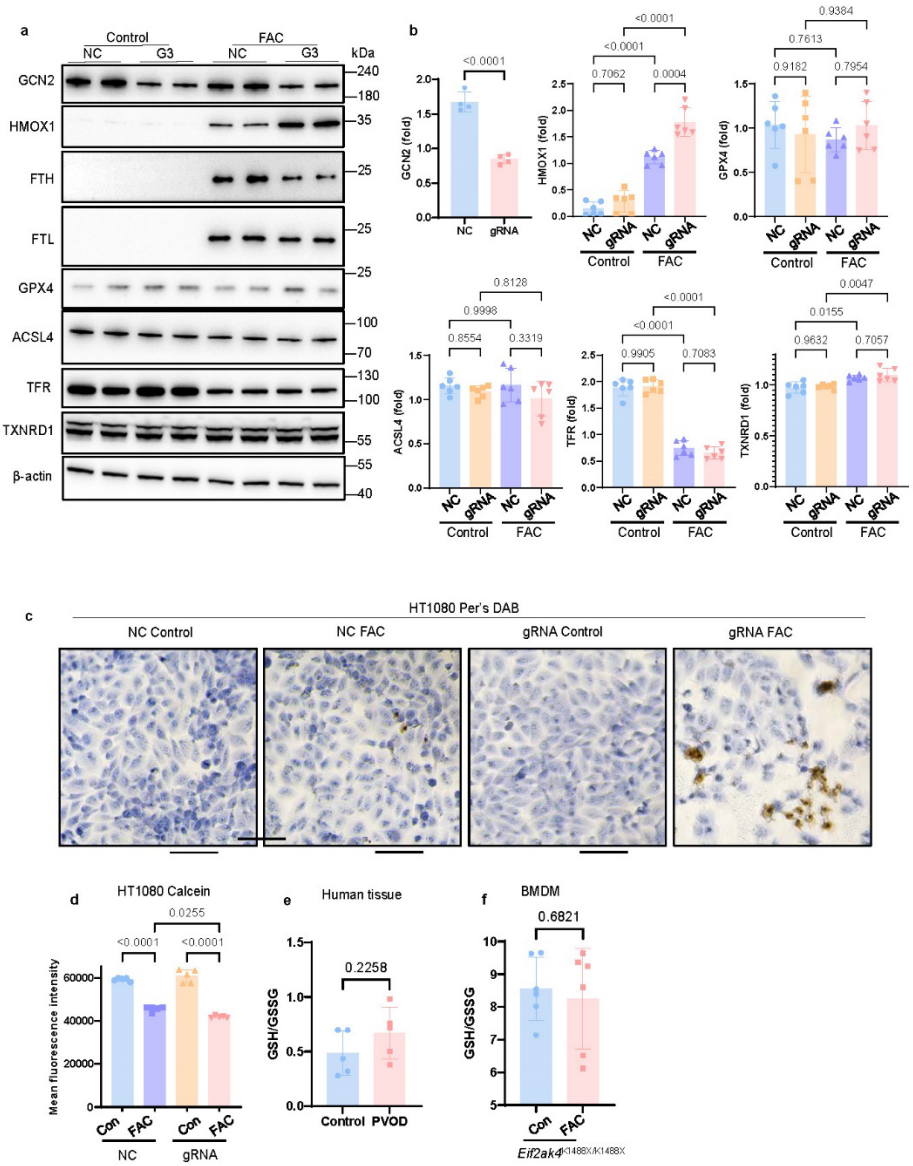

Figure S4. GCN2 deficiency sensitize BMDM/HT1080 to ferroptosis in the presence of iron.

a-b, WB showing expression levels of GCN2 in NC or GCN2$^{-/-}$ HT1080 cells. Data are the mean ± s.e.m., n=4, unpaired two-tailed t-test. WB analyzed expression levels of HMOX1, FTH, FTL, GPX4, ACSL4, TFRC, and TXNRD1 in NC or GCN2$^{-/-}$ HT1080 cells treated with/without 300 μM FAC 24 h. Data are the mean ± s.e.m., n=6, two-way ANOVA. **c**, Ferric iron deposits were stained with Perls' DAB staining in NC or GCN2$^{-/-}$ HT1080 cells treated with/without FAC 300 μM for 24h. Scale bar=50 μm. **d,** Mean fluorescence intensity of calcein assay in NC or GCN2$^{-/-}$ HT1080 treated with/without FAC 300 μM for 24h. Data are the mean ± s.e.m., n=5, two-way ANOVA. **e**, GSH/GSSG ratios in human control and PVOD lung tissues. Data are the mean ± s.e.m., n=5, unpaired two-tailed t-test. **f**, GSH/GSSG ratios in BMDM from *Eif2ak4*$^{K1488X/K1488X}$ mice, treated with/without 300 μM FAC 24 h. Data are the mean ± s.e.m., n=6, unpaired two-tailed t-test.

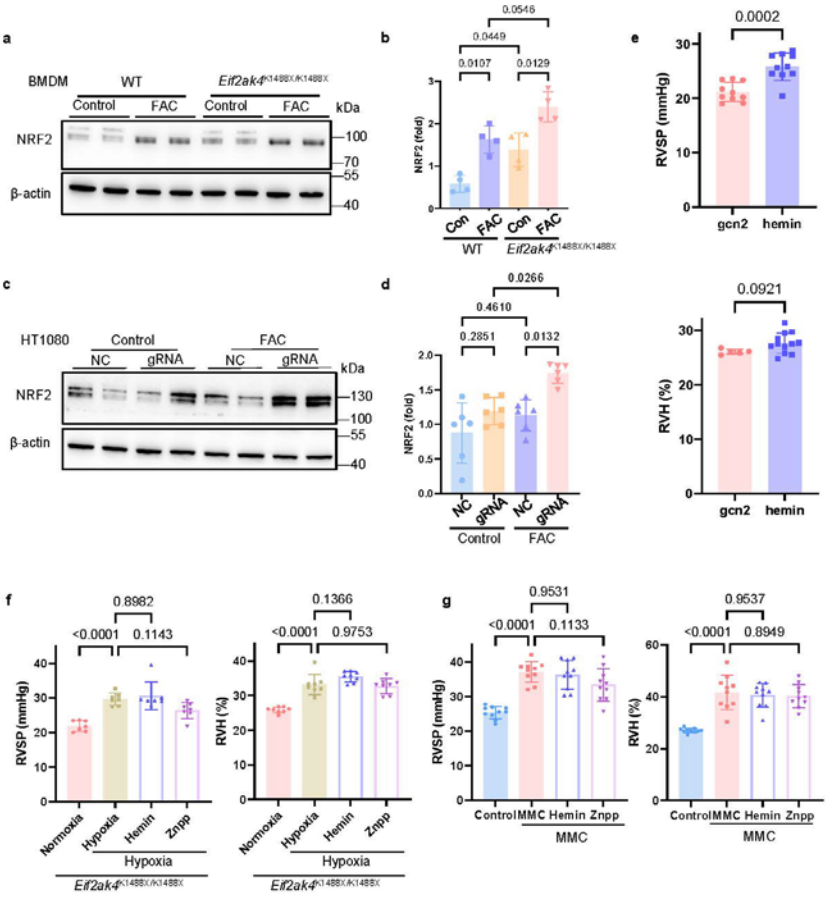

Figure S5. Iron treatment increased NRF2 in GCN2 deficiency cells, but HMOX1 modulators had no effect to prevent PVOD.

a-b, WB showing expression levels of NRF2 in WT or *Eif2ak4*$^{K1488X/K1488X}$ BMDMs treated with/without FAC 300 μM for 24h. Data are the mean ± s.e.m., n=4, two-way ANOVA. **c-d,** WB showing expression levels of NRF2 in NC or GCN2$^{-/-}$ HT1080 cells treated with/without FAC 300 μM for 24h. Data are the mean ± s.e.m., n=6, two-way ANOVA. **e**, Assessment of RVSP and RVH in *Eif2ak4*$^{K1488X/K1488X}$ (GCN2) mice treated with/without 25 mg/kg hemin 6 weeks. Data are the mean ± s.e.m., n=5-12, unpaired two-tailed t-test. **f**, Assessment of RVSP and RVH in *Eif2ak4*$^{K1488X/K1488X}$ mice under normoxia or hypoxia with/without 25 mg/kg hemin or 10 mg/kg Znpp 6 weeks. Data are the mean ± s.e.m., n=7-8, two-way ANOVA. **g,** Assessment of RVSP and RVH in control and MMC-induced rats with/without 25 mg/kg hemin or 10 mg/kg Znpp 5 weeks. Data are the mean ± s.e.m., n=10, two-way ANOVA.

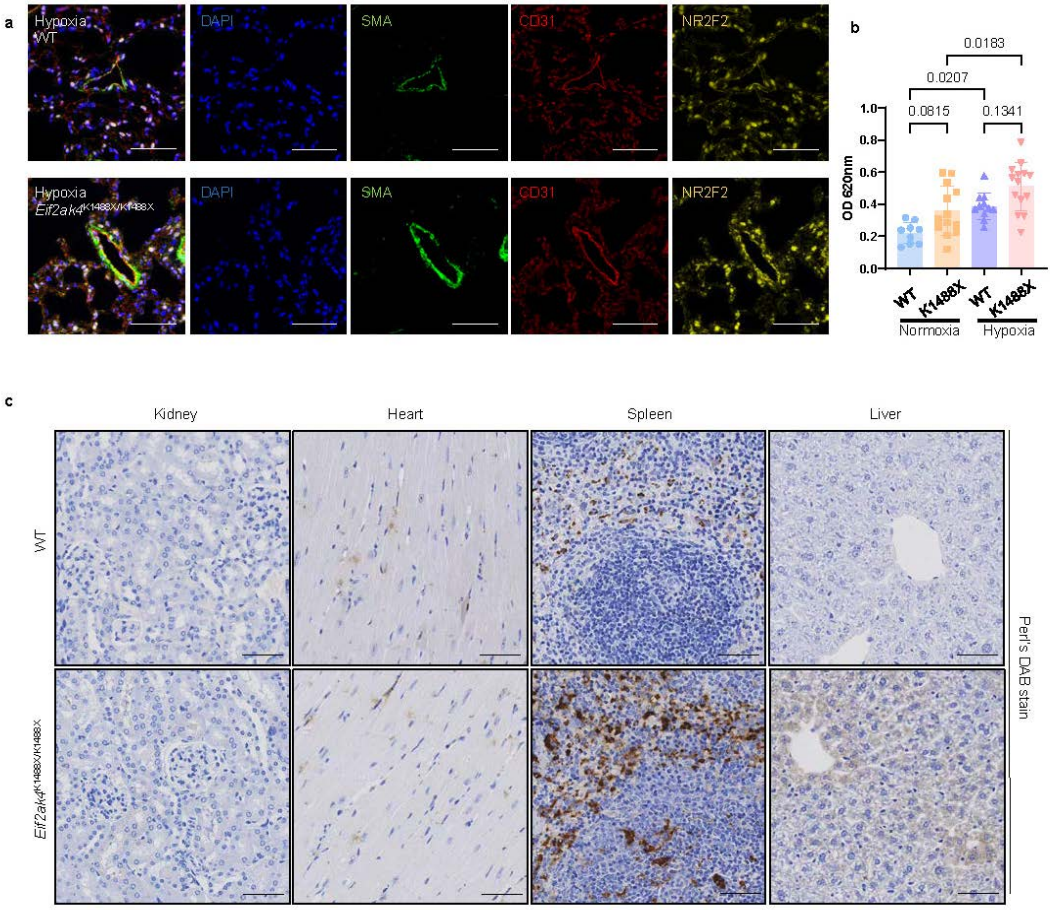

Figure S6. Leakage of endothelium in response to hypoxia and iron deposition in *Eif2ak4*$^{K1488X/K1488X}$ mouse lungs. **a**, Representative immunofluorescence staining images depict the expression levels of α-SMA (green), CD31 (red), and NR2F2 (yellow) in the lung tissues of WT and *Eif2ak4*$^{K1488X/K1488X}$ mice under hypoxia, with DAPI visualized in blue. Scale bar=50 μm. **b**, Wildtype (WT) and *Eif2ak4*$^{K1488X/K1488X}$ (K1488X) mice were treated with normoxia or hypoxia 6 weeks. Quantitative assessment of Evans blue dye content in the lungs of mice. Data are the mean ± s.e.m., n=9-14, two-way ANOVA. **c**, Ferric iron deposits were stained with Perls' DAB staining in WT and *Eif2ak4*$^{K1488X/K1488X}$ mice tissues. Scale bar=50 μm.

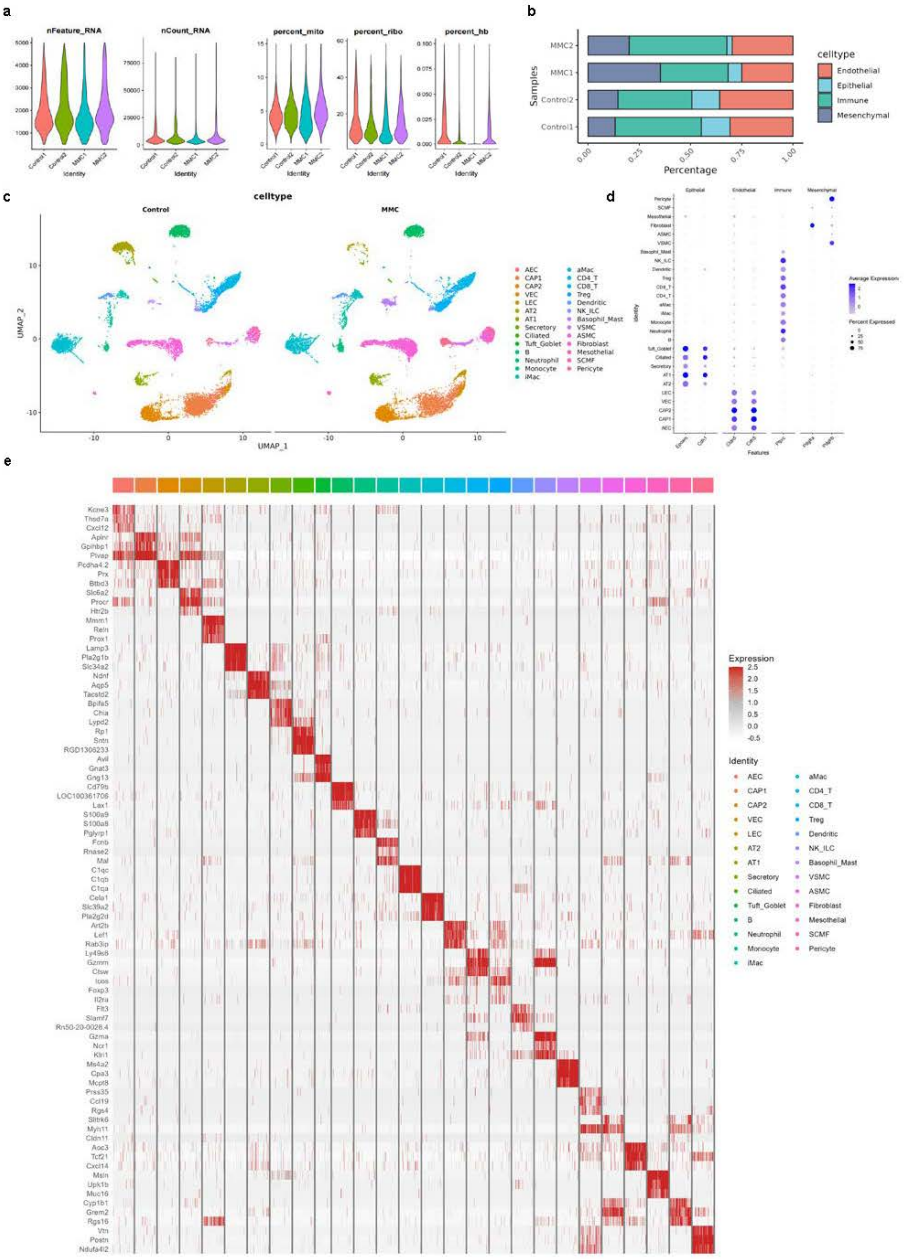

Figure S7. Quality control for control and MMC-induced rats scRNA-seq data.

a, Violin plots illustrating gene and UMI counts per droplet, along with the proportions of UMI counts associated with mitochondrial, ribosomal, and erythrocyte genes within each droplet. **b**, Stacked bar plots showing proportions of main cell types detected in control and MMC rat samples. **c**, UMAP plots of scRNA-seq data from control and MMC groups, annotated with cell type labels. **d**, Dot plot depicting the expression levels of endothelial, epithelial, immune, and mesenchymal markers across various cell types. **e**, Heatmap presenting the expression levels of the top 3 marker genes for each cell type, as determined by the COSG method.